INCOMPRESSIBLE FLOWS LINEAR STABILITY ANALYSIS

Master Research in Aerodynamics and Aeroacoustics

Global stability analysis of a 2D flow around an obstacle with porous surface

Supervisors:

Prof. Jean-Christophe Robinet

Prof. Chloé Mimeau

PhD Ricardo Frantz

Student:

Alessandro Luigi Castriotta

Academic year 2019/2020

Abstract

In this work, we would like to understand how a porous coating present on the surface of a solid obstacle modifies the flow dynamics. To do so, we use the linear stability analysis tool that allows us to see how the more important physical quantities of the flow are modified. In particular, in this thesis, we focus on the linear stability of the flow past a 2D porous square cylinder.
To take into account the porous layer in the mathematical model of the flow has been chosen the Brinkman Navier-Stokes equations. This is a very simple physical model because allows us to have different media in the whole domain only varying the value of the dimensionless penalization parameter λ. However, this model is valid only when the porosity of the porous medium is close to one ($\Phi \simeq 1$).
All the simulations are performed with the spectral elements code Nek5000. The results for the flow past a solid-porous obstacle obtained by Nek5000 are compared with the ones obtained by Hysop code which has already been validated in the context of porous flows. Through the stability tool, we have discovered, as we expected, that the bifurcation for the flow past an obstacle surrounded by a porous layer is delayed.

List of Figures

Contents

Chapter 1

Introduction

This work aims to carry out linear stability of two-dimensional incompressible flow around a 2D solid obstacle superposed by a porous layer. In particular, the obstacle is a square cylinder for which exists many studies and results in the literature [12], [4]. This study focuses on the first bifurcation of the flow, so for low Reynolds numbers. Adding the porous layer around the square cylinder, we will see how some properties of the flow will change. It is known that the use of porous coatings is a strategy that allows us to control and regularise the flow to modify the vortex shedding behind the obstacle and reduce the drag. This type of flow control is named **passive flow control**. The main advantage of the passive control method respect to the active method is that they are cheap and straightforward. The use of the porous coatings is not the only way to pursue the goal; in fact, in the literature has been proposed devices like the dimples [22], rough surface [20], splitter plates [21] to realize the passive flow control. When using porous coatings for flow control, one needs to take into account how efficiency is affected by the thickness, location, and permeability of the porous medium.
The porous medium plays an important role in the field of engineering, including Mechanical Engineering, Civil Engineering, Chemical Engineering, Material Engineering, Petroleum Engineering, and more. The applications in the industrial world of these particular materials are infinite: in fact, they are used to build a device for the heat transfer or storage, are analyzed to study the acoustic propagation in the structures, or are analyzed to study wavy propagation in earthquakes.
In the literature, many algorithms exist to model the flow through a porous medium. If we want to compute the flow past a porous interface, we can do it without resolving the porous flow using particular porous-fluid boundary conditions. However, this is an approximation, and in fact, many authors believe that for having a good description of the motion field it is necessary to solve the porous flow in the whole domain. The traditional way for doing this is to solve the coupling between the Darcy law and the Navier-Stokes equations. A more simple way to solve the whole porous flow is to use the **Brinkman model** that consists in adding a linear term to the right-hand side of the Navier-Stokes equations. This linear term is directly proportional to a coefficient, called the penalization factor, which specially prescribes the porosity and permeability of the different regions(solid, fluid, porous) of the domain. Bruneau and Mortazavi [5] were one of the first to propose the use of porous media to perform passive flow control by means of the penalization method with DNS.

In this internship, the linear stability analysis is used to try to understand how the addition of the porous layer may change the flow behavior and lead to passive flow control. It is noteworthy that the presence of the Brinkman term used to take into account the porous layer does not cause any additional difficulty to the stability analysis computation since the same is a linear term. Generally, the stability analysis provides the growth rate of σ and the frequency ω of the associated modes for a given control parameter (e.g., the Reynolds number). This means that for this configuration, one can know how the instability grows in time and at which frequency the flow oscillates. By repeating this procedure, one can map the parameter space and obtain precisely at parameter value the growth rate approximates zero, i.e., the **critical Reynolds number**. The critical value of the control parameter in which the flow bifurcates is crucial to understand and predict the change in behavior. Additionally, the computation of global modes can provide the spatial distribution of the perturbation, allowing a better insight into the effects of the porous layer.
The goal of this work is to see, through the results of linear stability analysis, how the flow dynamics is affected by the addition of the porous layer.In particular, questions such as: how the critical Reynolds number is affected with respect to a non-porous case ? How the global modes are modified? Does the position of the porous layer on the square cylinder can be used to break the flow symmetries?
This work is organized as follows: first, the mathematical model of the fluid dynamics equations are presented, i.e., the Navier-Stokes equations and the Brinkman equations for solving the porous flow. Then the numerical tools and algorithms for solving the stability problem will be shown. In the last chapter, the DNS and linear stability results on the solid square cylinder flow and the porous ones will be presented and discussed.

Chapter 2

Problem Formulation

2.1 Navier-Stokes equations

In fluid dynamics, the Navier-Stokes equations are a system of partial differential equations which govern the motion of viscous fluids; these equations are the mathematical formulation of the mass conservation principle, Newton's second law and the first law of thermodynamics.
The fluid dynamics equations are based on the continuum hypothesis which considers a fluid flow as a continuous system, thus ignoring the molecular nature of the fluid; since this work aims to perform a stability analysis of incompressible flow around a solid body, for which the effects of compressibility are negligible ($M \leq 0.3$), we will refer to the incompressible equations:

$$\begin{cases} \nabla \cdot \mathbf{u} = 0 \\ \rho \dfrac{\partial \mathbf{u}}{\partial t} + \rho(\mathbf{u} \cdot \nabla)\mathbf{u} = \nabla \cdot \mathbf{T} + \rho \mathbf{f} \end{cases} \tag{2.1}$$

where $\mathbf{u}$ is the velocity field, $\mathbf{T}$ is the stress tensor and $\mathbf{f}$ are the external forces; the first of equations (2.1) is the incompressibility constraint and the second is the momentum equation. If we decompose the stress tensor $\mathbf{T}$ as sum of an isotropic part due to pressure and a deviatoric part due to viscous stresses:

$$\mathbf{T} = \underbrace{-p\mathbf{I}}_{\text{Hydrostatic stress tensor}} + \underbrace{\boldsymbol{\tau}}_{\text{Viscous deviatoric stress tensor}} \tag{2.2}$$

and we make the hypothesis of **incompressible Newtonian fluid**, for which there is a linear relationship between viscous stress tensor $\boldsymbol{\tau}$ and deformation velocity tensor $\mathbf{E}$:

$$\boldsymbol{\tau} = 2\mu\mathbf{E} = \mu(\nabla \mathbf{u} + \nabla \mathbf{u}^T) \tag{2.3}$$

one obtains the mathematical formulation of the incompressible Navier-Stokes equations:

$$\begin{cases} \nabla \cdot \mathbf{u} = 0 \\ \rho \dfrac{\partial \mathbf{u}}{\partial t} + \rho(\mathbf{u} \cdot \nabla)\mathbf{u} = -\nabla p + \mu \Delta \mathbf{u} + \rho \mathbf{f} \end{cases} \tag{2.4}$$

where μ is the dynamic viscosity. As mentioned above, this equations represents physical principle at which fluids respond, as the momentum conservation; this can

be more clear if we analyze the various terms of the momentum equation:

$$\underbrace{\rho\frac{\partial \mathbf{u}}{\partial t} + \rho(\mathbf{u}\cdot\nabla)\mathbf{u}}_{\text{Inertial term}} = \underbrace{-\nabla p}_{\text{Pressure forces}} + \underbrace{\mu\Delta\mathbf{u}}_{\text{Viscous forces}} + \underbrace{\rho\mathbf{f}}_{\text{Volume forces}}$$

We can see clearly that the previous equation is a simple balance of forces, as stated in Newton's second law.

2.1.1 The dimensionless equations

In this section we will present the dimensionless formulation of equations (2.4); to do that, let us consider the following dimensionless quantity:

$$\mathbf{u}^* = \frac{\mathbf{u}}{U_\infty} \quad p^* = \frac{p}{\rho U_\infty^2} \quad \mathbf{x}^* = \frac{\mathbf{x}}{L} \quad t^* = \frac{tU_\infty}{L}.$$

where U_∞ is the free stream velocity and L is the characteristic body size; if one assume that there aren't external forces $\mathbf{f}$ exerced on the fluid, substituting this relationship in equations (2.4) one obtains:

$$\begin{cases} \nabla^*\cdot\mathbf{u}^* = \mathbf{0} \\ \dfrac{U_\infty^2\rho}{L}\dfrac{\partial \mathbf{u}^*}{\partial t^*} + \dfrac{U_\infty^2\rho}{L}(\mathbf{u}^*\cdot\nabla)\mathbf{u}^* = -\dfrac{U_\infty^2\rho}{L}\nabla^* p^* + \dfrac{\mu U_\infty}{L^2}\Delta^*\mathbf{u}^*. \end{cases}$$

Multiplying the second of the above equations by $\dfrac{L}{U_\infty^2\rho}$ one finally has:

$$\begin{cases} \nabla^*\cdot\mathbf{u}^* = 0 \\ \dfrac{\partial \mathbf{u}^*}{\partial t^*} + (\mathbf{u}^*\cdot\nabla)\mathbf{u}^* = -\nabla^* p^* + \dfrac{1}{Re}\Delta^*\mathbf{u}^*, \end{cases} \tag{2.5}$$

which correspond to the following four scalar equations:

$$\begin{cases} \dfrac{\partial u^*}{\partial x*} + \dfrac{\partial v^*}{\partial y*} + \dfrac{\partial w^*}{\partial z*} = 0 \\ \dfrac{\partial u^*}{\partial t*} + u^*\dfrac{\partial u^*}{\partial x*} + v^*\dfrac{\partial u^*}{\partial y*} + w^*\dfrac{\partial u^*}{\partial z*} = -\dfrac{\partial p^*}{\partial x^*} + \dfrac{1}{Re}\Delta^* u^* \\ \dfrac{\partial v^*}{\partial t*} + u^*\dfrac{\partial v^*}{\partial x*} + v^*\dfrac{\partial v^*}{\partial y*} + w^*\dfrac{\partial v^*}{\partial z*} = -\dfrac{\partial p^*}{\partial y^*} + \dfrac{1}{Re}\Delta^* v^* \\ \dfrac{\partial w^*}{\partial t*} + u^*\dfrac{\partial w^*}{\partial x*} + v^*\dfrac{\partial w^*}{\partial y*} + w^*\dfrac{\partial w^*}{\partial z*} = -\dfrac{\partial p^*}{\partial z^*} + \dfrac{1}{Re}\Delta^* w^*, \end{cases}$$

where $Re = LU_\infty/\nu$ is the Reynolds number, the ratio between the inertial and the viscous forces and $\nu = \mu/\rho$ the kinematic viscosity; the presence of the non-linear term $\mathbf{u}\cdot\nabla\mathbf{u}$ implies that the solution of the PDE system is highly dependent from the initial condition at fixed Reynlods number Re.
Even today there is no analytical solution to Navier-Stokes equations and the only thing one can do is to discretize the equations in space and time to obtain a numerical solution.
As one can see from equations (2.5), the Reynlods number is the only parameter that prescribes the dynamic of the flow.

2.2 Instability framework

The stability concept pertains to the tendency of a physical system to move away or not from its initial condition when this is perturbed. The system is said to be stable if an infinitesimal perturbation corresponds to a small variation of the present state which does not grow in time; otherwise, if the infinitesimal perturbation grow in time, the system is unstable.
The Navier-Stokes equations can be written, formally, as a dynamical system that evolves in time:

$$\frac{\partial \mathbf{q}}{\partial t} = \mathbf{F}(\mathbf{q}) \tag{2.6}$$

where $\mathbf{q}$ is the state vector and $\mathbf{F}$ is the non-linear operator. The first step to perform a stability analysis is to compute the base state of our problem; the base state $\mathbf{q}_s$ is a solution of the equation (2.6) such that:

$$\mathbf{F}(\mathbf{q}_s) = \mathbf{0} \Longleftrightarrow \frac{\partial \mathbf{q}_s}{\partial t} = \mathbf{0}$$

which means that the base state is a steady solution of the equations (2.6).
Now one is able to formalize from a mathematical point of view the stability analysis notion and so decompose the state vector $\mathbf{q}$ as a sum of a steady part $\mathbf{q}_s$ and a fluctuating part $\mathbf{q}'$:

$$\mathbf{q}(\mathbf{x}, t) = \mathbf{q}_s(\mathbf{x}) + \mathbf{q}'(\mathbf{x}, t) \tag{2.7}$$

Introducing the equation (2.7) into the (2.6), we obtain:

$$\frac{\partial(\mathbf{q}_s + \mathbf{q}')}{\partial t} = \mathbf{F}(\mathbf{q}_s + \mathbf{q}') \tag{2.8}$$

that is equivalent to:

$$\frac{\partial \mathbf{q}'}{\partial t} = \mathbf{F}(\mathbf{q}_s + \mathbf{q}')$$

because $\mathbf{q}_s$ is a steady solution of the equations (2.6):

$$\frac{\partial(\mathbf{q}_s + \mathbf{q}')}{\partial t} = \underbrace{\frac{\partial \mathbf{q}_s}{\partial t}}_{=0} + \frac{\partial \mathbf{q}'}{\partial t} = \frac{\partial \mathbf{q}'}{\partial t}$$

On the basis of equations (2.7) it is possible now to give some definitions about stability notion; suppose that a physical problem is governed by a set of partial differential equations (like NS equations) in a volume $\mathcal{V}$ and that the problem is closed by an initial condition at $t = 0$ and a set of boundary conditions on $\partial\mathcal{V}$.
One can define the amplitude of the perburbation $||\mathbf{q} - \mathbf{q}_s||$ such that:

$$||\mathbf{q} - \mathbf{q}_s||(t) = \left[\iiint_{\mathcal{V}} (\mathbf{q} - \mathbf{q}_s)^2 d\mathcal{V} \right]^{\frac{1}{2}} \tag{2.9}$$

Definition 2.2.1. *Lyapunov stability*
The base state $\mathbf{q}_s(\mathbf{x}, t)$ *is said to be stable if* $\forall \epsilon > 0, \exists \delta(\epsilon) > 0$ *such that if* $||\mathbf{q}(\mathbf{x}, 0) - \mathbf{q}_s(\mathbf{x}, 0)|| < \delta$ *then* $||\mathbf{q}(\mathbf{x}, t) - \mathbf{q}_s(\mathbf{x}, t)|| < \epsilon$, $\forall t \geq 0$.

The base state is stable if, for a given norm, it exists a limit for which the perturbations are small compared to the initial perturbation, $\forall t$. Now is given a more restrictive stability definition:

Definition 2.2.2. *Asymptotic stability*
The base state $\mathbf{q}_s(\mathbf{x}, t)$ *is said to be asymptotically stable if it is stable according to Lyapunov and* $\lim_{t\to\infty} ||\mathbf{q}(\mathbf{x}, t) - \mathbf{q}_s(\mathbf{x}, t)|| = 0$.

An even more restrictive definition is that of global stability:

Definition 2.2.3. *Global stability*
The base state $\mathbf{q}_s(\mathbf{x}, t)$ *is said to be unconditionally stable if it is stable and* $\forall ||\mathbf{q}(\mathbf{x}, 0) - \mathbf{q}_s(\mathbf{x}, 0)||$ one has $\lim_{t\to\infty} ||\mathbf{q}(\mathbf{x}, t) - \mathbf{q}_s(\mathbf{x}, t)|| = 0$.

A base state that is stable but not unconditionally stable is said to be conditionally stable, i.e. it exists an amplitude of the initial perturbation beyond which the base state is not asymptotically stable.
When the operator $\mathbf{F}$ is non-linear, there is not a general theory that allows to compute the non-linear stability; if the perturbation $\mathbf{q}'$ is "small" for a given base state $\mathbf{q}_s$, the equations can be linearized and in this case there is a complete theory on linear stability analysis.

Definition 2.2.4. *Linear Stability*
The base state $\mathbf{q}_s(\mathbf{x}, t)$ *is said to be stable if all infinitesimal perturbation evolving onto* $\mathbf{q}_s(\mathbf{x}, t)$ *decrease asymptotically.*

A base state that isn't linearly stable, is linearly unstable. Therefore, the definitions of linear stability are derived from more general definitions within the limit $\delta, \epsilon \to 0$.
If the flow is linearly asymptotically unstable, i.e. for δ small enough, then it is also asymptotically unstable.
Since in this work we will compute a global linear stability analysis for flow around a porous body, in the next section one will present the required mathematical tools to perform this study.

2.2.1 Linear analysis

In the theory of linear stability analysis, we assume that the perturbation is infinitesimal and so we can linearize the non-linear operator $\mathbf{F}$ around the steady state $\mathbf{q}_s$:

$$\mathbf{F}(\mathbf{q}) \simeq \underbrace{\mathbf{F}(\mathbf{q}_s)}_{=0} + \nabla\mathbf{F}(\mathbf{q}_s) \cdot (\mathbf{q} - \mathbf{q}_s) + \mathcal{O}(||\mathbf{q}||^2) \tag{2.10}$$

where $\nabla\mathbf{F}(\mathbf{q}_s)$ is a differential operator which depends on the base state $\mathbf{q}_s$; if we neglict the second order terms, equations (2.10) becomes:

$$\mathbf{F}(\mathbf{q}_s + \mathbf{q}') \simeq \nabla\mathbf{F}(\mathbf{q}_s) \cdot \mathbf{q}'.$$

Taking into account the previous considerations, equation (2.8) can be written as:

$$\frac{\partial \mathbf{q}'}{\partial t} = \nabla\mathbf{F}(\mathbf{q}_s) \cdot \mathbf{q}' \tag{2.11}$$

that is equivalent to the following form:

$$\begin{cases} \mathbf{B}\dfrac{\partial \mathbf{q}'}{\partial t} = \mathbf{J}\mathbf{q}' \\ \mathbf{q}'(\mathbf{x}, t=0) = \mathbf{q}'_0 \\ \mathcal{L}\mathbf{q}'(\mathbf{x}_0, t) = 0 \in \partial\mathcal{D} \end{cases} \tag{2.12}$$

which is the equation that governs the evolution in time of an infinitesimal perturbation $\mathbf{q}'$ with:

- $\mathbf{B}$ is a mass matrix;
- $\mathbf{J}$ is the Jacobian operator;
- $\mathbf{q}'_0$ is the initial condition;
- $\mathcal{L}\mathbf{q}'(\mathbf{x}_0, t)$ are the boundary conditions.

2.2.2 Linearized Navier-Stokes equations

With the mathematical tools presented in the previous section, we are now capable to linearize the Navier-Stokes equations around the base flow; if now we apply the decomposition (2.7) to the Navier-Stokes equations, one can write that:

$$\mathbf{u}(\mathbf{x}, t) = \mathbf{U}_b(\mathbf{x}) + \mathbf{u}'(\mathbf{x}, t)$$

$$p(\mathbf{x}, t) = p_b(\mathbf{x}) + p'(\mathbf{x}, t)$$

where $\mathbf{U}_b$ and p_b represents the steady solution of the Navier-Stokes equations (so the base flow) whereas $\mathbf{u}'$ and p' are the infinitesimal perturbations of the velocity field and pressure field.
Introducing the previous relationships in equations (2.5) one obtains:

$$\begin{cases} \nabla \cdot (\mathbf{U}_b + \mathbf{u}') = 0 \\ \dfrac{\partial(\mathbf{U}_b + \mathbf{u}')}{\partial t} + [(\mathbf{U}_b + \mathbf{u}') \cdot \nabla](\mathbf{U}_b + \mathbf{u}') = -\nabla(p_b + p') + \dfrac{1}{Re}\Delta(\mathbf{U}_b + \mathbf{u}') \end{cases}$$

If one now develops the calculus and recall that the base flow satisfy the following steady Navier-Stokes equations:

$$\begin{cases} \nabla \cdot \mathbf{U}_b = 0 \\ (\mathbf{U}_b \cdot \nabla)\mathbf{U}_b = -\nabla p_b + \dfrac{1}{Re}\Delta \mathbf{U}_b \end{cases} \tag{2.13}$$

one obtains:

$$\begin{cases} \nabla \cdot \mathbf{u}' = 0 \\ \dfrac{\partial \mathbf{u}'}{\partial t} + \underbrace{(\mathbf{U}_b \cdot \nabla)\mathbf{u}' + (\mathbf{u}' \cdot \nabla)\mathbf{U}_b}_{\text{Linear terms}} = -\nabla p' + \dfrac{1}{Re}\Delta \mathbf{u}' + \underbrace{(\mathbf{u}' \cdot \nabla)\mathbf{u}'}_{\text{Non-linear term}} \end{cases}$$

As one can see, these equations are still non-linear for the presence of the term $(\mathbf{u}' \cdot \nabla)\mathbf{u}'$.

If one suppose that the perturbation is infinitesimal (i.e. $||\mathbf{u}'|| << 1$) one can neglict the non-linear term obtaing the Linearized Navier-Stokes equations:

$$\begin{cases} \nabla \cdot \mathbf{u}' = 0 \\ \dfrac{\partial \mathbf{u}'}{\partial t} + (\mathbf{U}_b \cdot \nabla)\mathbf{u}' + (\mathbf{u}' \cdot \nabla)\mathbf{U}_b = -\nabla p' + \dfrac{1}{Re}\Delta \mathbf{u}' \end{cases} \tag{2.14}$$

which corresponds to the following scalar equations:

$$\begin{cases} \dfrac{\partial u'}{\partial x} + \dfrac{\partial v'}{\partial y} + \dfrac{\partial w'}{\partial z} = 0 \\ \dfrac{\partial u'}{\partial t} + U_b\dfrac{\partial u'}{\partial x} + V_b\dfrac{\partial u'}{\partial y} + W_b\dfrac{\partial u'}{\partial z} + u'\dfrac{\partial U_b}{\partial x} + v'\dfrac{\partial U_b}{\partial y} + w'\dfrac{\partial U_b}{\partial z} = -\dfrac{\partial p'}{\partial x} + \dfrac{1}{Re}\Delta u' \\ \dfrac{\partial v'}{\partial t} + U_b\dfrac{\partial v'}{\partial x} + V_b\dfrac{\partial v'}{\partial y} + W_b\dfrac{\partial v'}{\partial z} + u'\dfrac{\partial V_b}{\partial x} + v'\dfrac{\partial V_b}{\partial y} + w'\dfrac{\partial V_b}{\partial z} = -\dfrac{\partial p'}{\partial y} + \dfrac{1}{Re}\Delta v' \\ \dfrac{\partial w'}{\partial t} + U_b\dfrac{\partial w'}{\partial x} + V_b\dfrac{\partial w'}{\partial y} + W_b\dfrac{\partial w'}{\partial z} + u'\dfrac{\partial W_b}{\partial x} + v'\dfrac{\partial W_b}{\partial y} + w'\dfrac{\partial W_b}{\partial z} = -\dfrac{\partial p'}{\partial z} + \dfrac{1}{Re}\Delta w' \end{cases}$$

The previous system can be written as system (2.12) introducing the mass matrix $\mathbf{B}$ and the Jacobian operator $\mathbf{J}$:

$$\mathbf{B} = \begin{pmatrix} \mathbf{I} & 0 \\ 0 & 0 \end{pmatrix} \qquad \mathbf{J} = \begin{pmatrix} -\nabla \mathbf{U}_b - \mathbf{U}_b \cdot \nabla + \mathrm{Re}^{-1}\Delta & -\nabla \\ \nabla \cdot & 0 \end{pmatrix}$$

obtaining so the compact form of the equations (2.14).

2.2.3 Global linear stability analysis

If the base flow $\mathbf{U}_b$ is steady, the linearized Navier-Stokes equations are autonomous and so the solution can be found as a normal mode:

$$\mathbf{q}'(\mathbf{x}, t) = \hat{\mathbf{q}}(\mathbf{x})e^{\psi t} \tag{2.15}$$

Introducing this formulation for $\mathbf{q}'$ in the equations (2.14) we obtain:

$$\begin{cases} \nabla \cdot \hat{\mathbf{u}} = 0 \\ \psi\hat{\mathbf{u}} + (\mathbf{U}_b \cdot \nabla)\hat{\mathbf{u}} + (\hat{\mathbf{u}} \cdot \nabla)\mathbf{U}_b = -\nabla \hat{p} + \dfrac{1}{Re}\nabla^2\hat{\mathbf{u}} \end{cases}$$

and recalling the mass matrix $\mathbf{B}$ and the Jacobian operator $\mathbf{J}$ one can write the previous equation in the following eingenvalues problem:

$$\psi\mathbf{B}\hat{\mathbf{q}} = \mathbf{J}\hat{\mathbf{q}} \Longleftrightarrow \{\mathbf{J} - \psi\mathbf{B}\}\hat{\mathbf{q}} = \mathbf{0} \tag{2.16}$$

where $\psi = \sigma + i\omega$ is the eigenvalue and $\hat{\mathbf{q}}$ is the eigenvector associated to the eigenproblem (2.16); it is important to underline that the eigenvalues represent the global modes of the base flow $\mathbf{U}_b$ and that the real part σ of the leading eigenvalue is the growth rate of the instability whereas the imaginary part ω characterises the stationary or oscillatory nature of the associated eigenvector; indeed, if we introduce the eigenvalues in the equation (2.15) one obtain:

$$\mathbf{q}'(\mathbf{x}, t) = \hat{\mathbf{q}}(\mathbf{x})e^{\sigma t}e^{i\omega t} \tag{2.17}$$

As one can see, the sign of the growth rate σ determines the stability of the base flow $\mathbf{U}_b$:

- if $\sigma < 0$ the perturbation decays exponentially in time and the base flow $\mathbf{U}_b$ is globally stable;
- is $\sigma > 0$ the perturbation grows exponentially in time and the base flow $\mathbf{U}_b$ is globally unstable.

2.3 The penalization method

In this work, we want to model fluid flow in a domain constituted of three different media (a solid, a saturated porous medium and an incompressible fluid) with the same equation using the penalization method. The penalization method consists in add a forcing term on the right hand side of the momentum equations and thanks to this term, it is possible to model the entire domain as a porous medium with different permeabilities.

2.3.1 The Brinkman Navier-Stokes equations

We recall that the three-dimensional formulation of the Navier-Stokes equations, without external forces, is given by:

$$\begin{cases} \nabla \cdot \mathbf{u} = 0 \\ \rho \dfrac{\partial \mathbf{u}}{\partial t} + \rho(\mathbf{u} \cdot \nabla)\mathbf{u} = -\nabla p + \mu \Delta \mathbf{u} \end{cases}$$

where ρ is the fluid density, μ is the dynamic viscosity of the fluid, $\mathbf{u}$ is the velocity vector field and p is the pressure scalar field.
The flow velocity $\mathbf{u}$ in a porous medium is given by the **Darcy law**:

$$\mathbf{u} = -\frac{k}{\mu \Phi} \nabla p \tag{2.18}$$

where Φ denotes the porosity of the medium and k is the intrinsic permeability.
The **porosity** Φ of a porous medium corresponds to the fraction of void space in a material and it is defined as follows:

$$\Phi = \frac{V_V}{V_T} \tag{2.19}$$

where V_V indicates the volume of the void-space and V_T is the total volume of the material, including the solid and the void parts. The porosity is therefore a value between 0 and 1.
The **permeability** k measures the ability of a porous material to allow fluids to pass through it. High permeabilities will therefore enable a fluid to evolve fastly within a porous medium. This quantity directly derives from the Darcy equation and its unit of measure is the darcy ($D_a = 0.97 \times 10^{-12} m^2$).
If we assume that the Boussinesq hypothesis is satisfied for the fluid saturating the porous medium, we get the Brinkman equation:

$$\nabla p = -\frac{\mu \Phi}{k} \mathbf{u} + \tilde{\mu} \Phi \Delta \mathbf{u} \tag{2.20}$$

where $\tilde{\mu}$ is the Brinkman's effective viscosity. Is a common practice to set μ equal to $\tilde{\mu}$ when we have high porosity ($\Phi \sim 1$); therefore, assuming that $\tilde{\mu} \sim \mu/\Phi$, equation (2.20) becomes:

$$\nabla p = -\frac{\mu\Phi}{k}\mathbf{u} + \mu\Delta\mathbf{u}$$

If we add the intertial terms to the previous equation we obtain the Brinkman Navier-Stokes equations [5]:

$$\begin{cases} \nabla \cdot \mathbf{u} = 0 \\ \dfrac{\partial \mathbf{u}}{\partial t} + (\mathbf{u}\cdot\nabla)\mathbf{u} = -\dfrac{\nabla p}{\rho} - \dfrac{\mu\Phi}{k\rho}\chi_b\mathbf{u} + \dfrac{\mu}{\rho}\Delta\mathbf{u} \end{cases} \tag{2.21}$$

where χ_b is the characteristic function equal to 0 in the fluid and 1 in the body. It is important to recall that the Brinkman equation is only valid when the porosity is close to one ($\Phi \simeq 1$).

2.3.2 The dimensionless equation

To obtain the dimensionless formulation of equations (2.21), let us consider the following dimensionless quantities:

$$\mathbf{u}^* = \frac{\mathbf{u}}{U_\infty} \quad p^* = \frac{p}{\rho U_\infty^2} \quad \mathbf{x}^* = \frac{\mathbf{x}}{L} \quad t^* = \frac{tU_\infty}{L}.$$

Substituting this relationship in equations (2.21) one obtains:

$$\begin{cases} \nabla^* \cdot \mathbf{u}^* = \mathbf{0} \\ \dfrac{U_\infty^2}{L}\dfrac{\partial \mathbf{u}^*}{\partial t^*} + \dfrac{U_\infty^2}{L}(\mathbf{u}^*\cdot\nabla)\mathbf{u}^* = -\dfrac{U_\infty^2}{L}\nabla^* p^* + \dfrac{\mu U_\infty}{L^2\rho}\Delta^*\mathbf{u}^* - \dfrac{\mu\Phi U_\infty}{k\rho}\chi_b\mathbf{u}^*, \end{cases}$$

and multiplying the second of the above equations by $\dfrac{L}{U_\infty^2}$ one finally has:

$$\begin{cases} \nabla^* \cdot \mathbf{u}^* = 0 \\ \dfrac{\partial \mathbf{u}^*}{\partial t^*} + (\mathbf{u}^*\cdot\nabla)\mathbf{u}^* = -\nabla^* p^* + \dfrac{1}{Re}\Delta^*\mathbf{u}^* - \lambda\chi_b\mathbf{u}^*, \end{cases} \tag{2.22}$$

where $\lambda = 1/K = \mu\Phi L/k\rho U_\infty = \Phi L^2/kRe$ is the dimensionless penalization parameter that is directly linked to the porosity Φ and to the intrinsic permeability of the medium k.

When there is a fluid-solid-porous interaction the behavior and properties of the flow change; in particular from a physical point of view, one can understand what happens at the flow velocity profile looking at the figure 2.1. As explained in [6] by Bruneau and Mortazavi, one can consider five regions from the solid wall to the freestream fluid flow.

Region 1 corresponds to the thickness of the boundary layer close to the solid wall while in the region 2 the flow velocity $\mathbf{u}_D$ is uniform ($\mathbf{u}_D$ is the Darcy velocity). Regions 3 and 4 are two transient layers where the velocity growth, respectively, from $\mathbf{u}_D$ to $\mathbf{u}_i$ and from $\mathbf{u}_i$ to $\mathbf{u}_\infty$. As mentioned above, the penalization method allows us to consider the whole domain as a porous medium with different permeabilities.

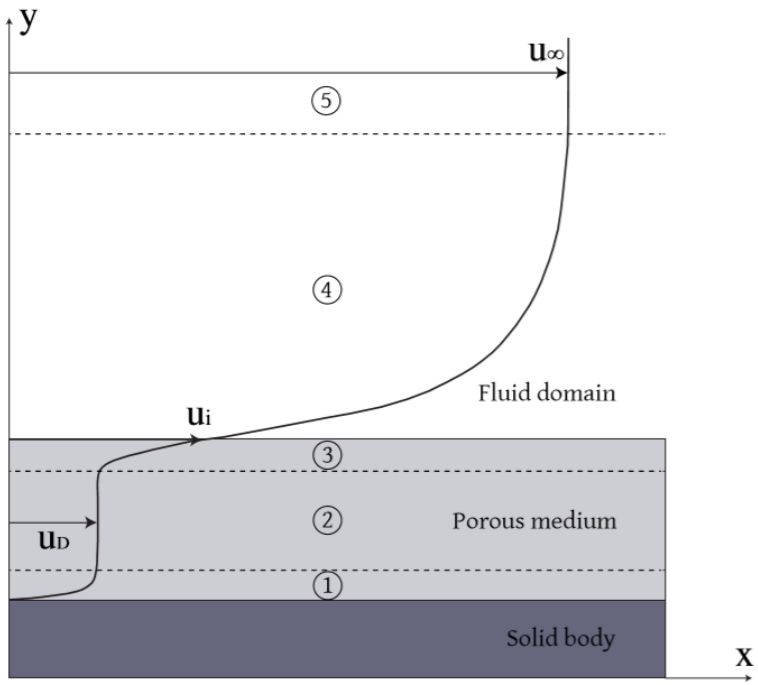

Figure 2.1: Velocity profile in a porous media. $\mathbf{u}_D$ denotes the Darcy velocity inside the porous media, $\mathbf{u}_i$ is the slip velocity and $\mathbf{u}_\infty$ is the freestream velocity. Figure from Mimeau thesis [15].

In this work we set $L = \rho = U_\infty = 1$ and therefore, at given Reynolds number, the penalization parameter λ only depends, in the inverse proportion, to the intrinsic permebeality of the medium k. Let us note that this model is valid only when the porosity of the porous medium Φ is close to one. Varying the value of λ thus directly defines the different media. Indeed, in the fluid, the intrinsic permeability coefficient k goes to infinity ($k \to \infty$), thus the fluid can be considered as a porous media with a very high permeability. So if we set $\lambda = 0$ in this region the penalization term vanishes in equation (2.22) and we naturally recover the dimensionless Navier-Stokes equations:

$$\begin{cases} \nabla^* \cdot \mathbf{u}^* = 0 \\ \dfrac{\partial \mathbf{u}^*}{\partial t^*} + (\mathbf{u}^* \cdot \nabla)\mathbf{u}^* = -\nabla^* p^* + \dfrac{1}{Re}\Delta^* \mathbf{u}^*. \end{cases}$$

If the intrinsic permeability k goes to zero ($k \to 0$), we can consider this region as a solid medium and set λ to very high value, for example $\lambda \simeq 10^8$. It was proved by [2] that solving equations (2.22) with such value of λ is equivalent to solve Darcy's law in a solid. Finally, for an intermediate value of λ, between 0 and 10^8, one can consider this region as a porous medium in which the flow has a Darcy velocity $\mathbf{u}_D$. The next table will summarize what has been said about the λ parameter and the consequent flow behavior.

Domain regions	λ-value and corresponding permeability	State of the velocity flow
Fluid	$\lambda = 0$ (infinite permeability)	$\mathbf{u}$ is not penalized
Solid	$\lambda = 10^8$ (zero permeability)	$\mathbf{u} \to 0$
Porous	$0 < \lambda < 10^8$ (intermediate permeability)	$\mathbf{u} = \mathbf{u}_D$

Chapter 3

Numerical tools

3.1 Nek5000

The work of this internship has been based on the use of the spectral elements code Nek5000 [8] for developing every step of the linear stability analysis; the code is written in f77 and C and allows to simulate laminar, transitional, and turbulent incompressible or low Mach-number flows with heat transfer. The code is based on the Nekton 2.0 spectral element code written by Paul Fischer, Lee Ho and Einar Rønquist in 1986-1991, with technical input from A.Patera and Y.Maday; the development of the code Nek5000 has been carried out in the last thirty years by P.Fischer et al. and today it is used by hundreds of scientists and engineers in academia, laboratories and industry. [1]
In this chapter, we will present first a brief presentation of time integration and spatial discretization that is used in Nek5000 and after the Selective Frequency Damping method for the base flow computation and finally the Arnoldi algorithm for solving the eigenvalues problem; for more details about the numerical method see chapter 6 of Nek5000 documentation [1].

3.1.1 Time integration

In this section we will present the temporal discretization used by Nek5000 [8] for the incompressible Navier-Stokes equations:

$$\begin{cases} \nabla \cdot \mathbf{u} = 0 \\ \dfrac{\partial \mathbf{u}}{\partial t} + \mathbf{u} \cdot \nabla \mathbf{u} = -\nabla p + \dfrac{1}{Re} \Delta \mathbf{u} \end{cases}$$

For stability reasons we will treat the non-linear terms via an explicit method and the linear term via an implicit method; we can rewrite the momentum equation by denoting the non-linear term as $\mathbf{N}(\mathbf{u})$ and the linear one as $\mathbf{L}(\mathbf{u})$:

$$\frac{\partial \mathbf{u}}{\partial t} = -\nabla p + \mathbf{N}(\mathbf{u}) + \mathbf{L}(\mathbf{u})$$

where $\mathbf{N}(\mathbf{u}) = -\mathbf{u} \cdot \nabla \mathbf{u}$ and $\mathbf{L}(\mathbf{u}) = \dfrac{1}{Re} \Delta \mathbf{u}$.

[1] from https://www.mcs.anl.gov/~fischer/nek5000/primer.pdf

One can discretize the equation using a k-th order backward differentation formula that approximates the derivative $\dfrac{\partial \mathbf{u}}{\partial t}$:

$$\sum_{j=0}^{k} \frac{b_j}{\Delta t}\mathbf{u}^{n+1-j} = -\nabla p^{n+1} + \mathbf{N}(\mathbf{u}^{n+1}) + \mathbf{L}(\mathbf{u}^{n+1}) \tag{3.1}$$

and extrapolating the non-linear term as:

BDFk				
k	b_0	b_1	b_2	b_3
1	1	-1		
2	$\frac{3}{2}$	$-\frac{4}{2}$	$\frac{1}{2}$	
3	$\frac{11}{6}$	$-\frac{18}{6}$	$\frac{9}{6}$	$-\frac{2}{6}$

Table 3.1: Coefficients for the k-order backward finite difference scheme with $k \leq 3$.

$$\mathbf{N}(\mathbf{u}^{n+1}) = \sum_{j=1}^{k} a_j \mathbf{N}(\mathbf{u}^{n+1-j})$$

we have:

EXTk			
k	a_1	a_2	a_3
1	1		
2	2	-1	
3	3	-3	1

Table 3.2: Coefficients for the k-order extrapolation scheme with $k \leq 3$.

$$\sum_{j=0}^{k} \frac{b_j}{\Delta t}\mathbf{u}^{n+1-j} = -\nabla p^{n+1} + \sum_{j=1}^{k} a_j \mathbf{N}(\mathbf{u}^{n+1-j}) + \mathbf{L}(\mathbf{u}^{n+1}) \tag{3.2}$$

If now we separate the implicit and explicit term:

$$\frac{b_0}{\Delta t}\mathbf{u}^{n+1} + \nabla p^{n+1} - \mathbf{L}(\mathbf{u}^{n+1}) = \underbrace{-\sum_{j=1}^{k} \frac{b_j}{\Delta t}\mathbf{u}^{n+1-j} + \sum_{j=1}^{k} a_j \mathbf{N}(\mathbf{u}^{n+1-j})}_{\mathbf{F}(\mathbf{u}^n)} \tag{3.3}$$

that is equivalent to:

$$\frac{b_0}{\Delta t}\mathbf{u}^{n+1} + \nabla p^{n+1} - \Delta \mathbf{u}^{n+1} = \mathbf{F}(\mathbf{u}^n) \tag{3.4}$$

where the term $\mathbf{F}(\mathbf{u}^n)$ is an explicit term that can be calculated using information known at the previous time t^n.

3.1.2 Spatial discretization

Since nowadays it is not possible to compute an analytical solution of Navier-Stokes equations, it is necessary to discretize the equations to obtain a numerical solution. The code Nek5000 [8] used in this internship work, is based on the Legendre spectral elements method, that was introduced by in 1984 by A. Patera [18]. This method shares many features with the finite element method and therefore it is included in the family of approximation schemes based on Garlekin's method. The idea which is based Nek5000 is to minimize the error of the numerical computation in the energy norm over a chosen space of polynomials of order N. For further details, the reader is referred to the books by Deville *et al* [7].

3.2 Base flow computation

In the theory of linear stability, the first step is the computation of the fixed points of Navier-Stokes equations around which the equations will then be linearized. After their computation, linear stability will tell us if the fixed points are stable or not. For this internship work, we chose the Selective Frequency Damping (SFD) method, a simple numerical approach used to calculate the steady state of an unstable configuration that was first proposed by Åkervik et al.(2006) [23].

3.2.1 Selective frequency damping

In this paragraph will be present as the *Selective Frequency Damping* method works; we recall that the Navier-Stokes equations can be written as:

$$\dot{\mathbf{q}} = \mathbf{F}(\mathbf{q}) \tag{3.5}$$

The main idea of the SFD method is to introduce a linear forcing term in the right hand side of equation (3.5); doing that the new problem formulation is:

$$\dot{\mathbf{q}} = \mathbf{F}(\mathbf{q}) - \chi(\mathbf{q} - \mathbf{q}_s) \tag{3.6}$$

One can observe that when $\mathbf{q}_s$ is a steady solution of equation (3.6),then $\mathbf{q}_s$ is also steady solution of equation (3.5); the problem is that this steady solution $\mathbf{q}_s$ is not known a priori. The SFD method replaces this unknown steady state $\mathbf{q}_s$ by a low-pass filtered version of $\mathbf{q}$, denoted $\bar{\mathbf{q}}$. To close the system it is necessary to add an equation that governs the evolution in time of low-pass filtered solution $\bar{\mathbf{q}}$; doing that the new formulation of equation (3.6) is:

$$\begin{cases} \dot{\mathbf{q}} = \mathbf{F}(\mathbf{q}) - \chi(\mathbf{q} - \bar{\mathbf{q}}) \\ \dot{\bar{\mathbf{q}}} = \omega_c(\mathbf{q} - \bar{\mathbf{q}}) \end{cases} \tag{3.7}$$

which, in the case of the Navier-Stokes equations becomes:

$$\begin{cases} \dot{\mathbf{u}} + (\mathbf{u} \cdot \nabla)\mathbf{u} = -\nabla p + \dfrac{1}{Re}\Delta\mathbf{u} - \chi(\mathbf{u} - \bar{\mathbf{u}}) \\ \dot{\bar{\mathbf{u}}} = \omega_c(\mathbf{u} - \bar{\mathbf{u}}) \\ \nabla \cdot \mathbf{u} = 0 \end{cases} \tag{3.8}$$

where χ is the gain of the filter and ω_c its cut-off circular frequency. The choice of these two parameters is very important: χ has to be positive and greater than the growth rate of the instability one aims to kill, whereas ω_c has to be lower than the eigenfrequency ω of the instability (usually $\omega_c = \omega/2$); for more details about this see [11].

3.3 Eigenvalues problem computation

As seen in the previous sections, the linear stability problem requires the eigenspectra computation of the Jacobian operator $\mathbf{J}$; nowadays different algorithm exist for the computation of the eigenpairs $(\hat{\mathbf{q}}, \psi)$ but unfortunately, these requires the storage of the mass matrix $\mathbf{B}$ and the Jacobian operator $\mathbf{J}$; this can rapidly become a limitation because the generalized eigenproblem (2.16) comes directly from the discretization of the fully linearized Navier-Stokes equations (LNSE) that involves a very large number of degrees of freedom and so the storage of the mass matrix $\mathbf{B}$ and the Jacobian operator $\mathbf{J}$ would be highly expensive.
To avoid this complication, different algorithms have been proposed in the past; the one that has been used in this internship work is based on a time-stepper approach of the eigenvalues problem as proposed initially by Marcus Tuckerman [14] in 1987.

3.3.1 Time-stepper approach

The idea of this method is to project our linear dynamical system into a divergence-free vector space such that equations (2.14) can be rewritten as:

$$\frac{\partial \mathbf{u}'}{\partial t} = \mathbf{A}\mathbf{u}' \tag{3.9}$$

where now $\mathbf{A}$ is the projected Jacobian operator; one can observe that equation (3.9) accepts a solution as:

$$\mathbf{u}'(\Delta t) = \mathbf{u}'_0 \underbrace{e^{\mathbf{A}\Delta t}}_{\mathbf{M}(\Delta t)} \tag{3.10}$$

where the term $e^{\mathbf{A}\Delta t}$ is called the exponential propagator $\mathbf{M}(\Delta t)$ of equation (3.9). At first sight, it would seem the operation is counterproductive since the size of the matrix has remained unchanged, as the calculation of an exponential matrix $e^{\mathbf{A}\Delta t}$ can computationally demanding. It is noteworthy that this operation can be approximated with the action of the exponential propagator $\mathbf{M}(\Delta t)$ on a vector $\mathbf{u}'_0$. This is achieved by time-marching the LNSE from an appropriate initial condition $\mathbf{u}'_0$; a secondary aspect relies on the fact that eigenpairs $(\mathbf{V}, \Lambda)$ of the projected Jacobian matrix $\mathbf{A}$ and the eigenpairs $(\mathbf{V}_e, \Sigma)$ of the exponential propagator $\mathbf{M}(\Delta t)$ are simply related by relationships:

$$\Lambda = \frac{\log(\Sigma)}{\Delta t}, \quad \mathbf{V} = \mathbf{V}_e \tag{3.11}$$

These considerations therefore lead us to calculate the eigenpairs of the exponential propagator $\mathbf{M}(\Delta t)$ that those of the Jacobian operator $\mathbf{A}$; through a simple logarithmic conversion it is possible to calculate the eigenvalues of $\mathbf{A}$.

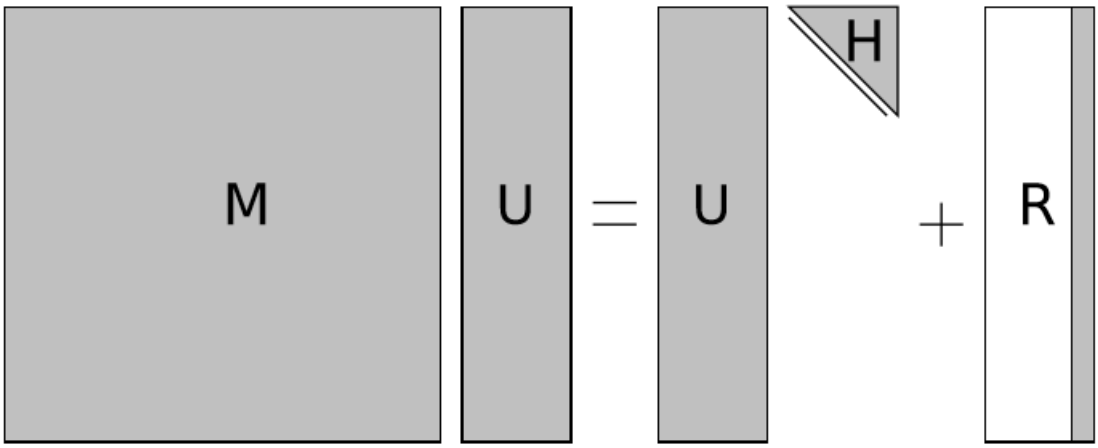

Figure 3.1: The *Arnoldi iteration*: given a square matrix $\mathbf{M} \in \mathbb{R}^{n\times n}$, construct $\mathbf{U} \in \mathbb{R}^{n\times k}$ with orthonormal columns such that $\mathbf{H} \in \mathbb{R}^{k\times k}$ is an upper Hessenberg matrix and only the last column of the residual $\mathbf{R} \in \mathbb{R}^{n\times k}$ is non zero. Figure adapt from [3].

3.3.2 Arnoldi algorithm

The Arnoldi algorithm combines the properties of the power iteration method and of the Gram-Schmidt iterations to find an approximation to the leading eigenvalues and eigenvectors of matrix $\mathbf{M}$ to constructing an orthonormal basis of the Krylov subspace with dimension n:

$$\mathbf{K}_n = \left\{\mathbf{u}_0, \mathbf{M}\mathbf{u}_0, ..., \mathbf{M}^{n-1}\mathbf{u}_0\right\} \tag{3.12}$$

where $\mathbf{M}$ is the exponential propagator and $\mathbf{u}_0$ is an initial arbitrary vector such that $||\mathbf{u}_0|| = 1$; the sequence (3.12) forms the so-called Krylov subspace.
The power iteration method is a simple algorithm that produces a number ψ, which is the greatest eigenvalue of a matrix $\mathbf{A}$ and a vector $\mathbf{v}$, that is the corresponding eigenvector, such that $\mathbf{A}\mathbf{v} = \psi\mathbf{v}$; however, it only uses the last result of the sequence (3.12), losing potentially important information of the previous iterations; alternatively the Arnoldi algorithm uses all the information of the sequence (3.12) thanks to a Gram-Schimdt iteration that orthogonalize the vectors.
The basic Arnoldi iteration is characterized by the following relationship:

$$\mathbf{M}\mathbf{U}_k = \mathbf{U}_k\mathbf{H}_k + \mathbf{r}_k\mathbf{e}_k^T \tag{3.13}$$

where $\mathbf{U}_k$ is a set of orthonormal vector, $\mathbf{H}_k$ is an upper Hessenberg matrix and $\mathbf{r}_k$ is a residual vector that indicates how far is $\mathbf{U}_k$ from an invariant subspace of $\mathbf{M}$; the determination of the upper Hessenberg matrix $\mathbf{H}$ is performed according to the Arnoldi algorithm, where the computation of the $\mathbf{w} = \mathbf{M}\mathbf{u}_j$ is actually performed numerically by time-marching the LNSE; figure 3.1 shows the matrices involved in the algorithm. The eigenpairs of the upper Hessenberg matrix $(\Sigma_H, \mathbf{X})$ can be computed easly and are a good approximation of those of $\mathbf{M}$; indeed, this upper Hessenberg matrix is a low-dimensional approximation of the exponential propagator $\mathbf{M}$ and its eigenpairs are linked to the eigenpairs of the Jacobian matrix $\mathbf{A}$ by the

following relationship:

$$\begin{cases} \Lambda = \sigma + i\omega \simeq \dfrac{\log(\Sigma_H)}{\Delta t} \\ \mathbf{V} \simeq \mathbf{UX} \end{cases}$$

where Δt is the sampling period; we must underline that this technique is the result of a sophisticated treatment of the signal and therefore in order to have acceptable results we must respect the Nyquist criterion. Finally, the Arnoldi algorithm used in this internship work is showed in the figure 3.2.

Algorithm 1 The k-step *Arnoldi* factorisation.

Require: $\mathbf{M} \in \mathbb{R}^{n \times n}$, starting vector $\mathbf{u} \in \mathbb{R}^n$.

$\mathbf{u}_1 = \mathbf{u}/\|\mathbf{u}\|$;
$\mathbf{w} = \mathbf{M}\mathbf{u}_1$;
$\alpha_1 = \mathbf{u}_1^T \mathbf{w}$;
$\mathbf{f}_1 \leftarrow \mathbf{w} - \alpha_1 \mathbf{u}_1$;
$\mathbf{U}_1 \leftarrow (\mathbf{u}_1)$;
$\mathbf{H}_1 \leftarrow (\alpha_1)$;
for $j = 1, 2, \cdots, k-1$ **do**
  $\beta_j = \|\mathbf{f}_j\|$;
  $\mathbf{u}_{j+1} \leftarrow \mathbf{f}_j/\beta_j$;
  $\mathbf{U}_{j+1} \leftarrow (\mathbf{U}_j, \mathbf{u}_{j+1})$;
  $\hat{\mathbf{H}}_j \leftarrow \begin{pmatrix} \mathbf{H}_j \\ \beta_j \mathbf{e}_j^T \end{pmatrix}$
  $\mathbf{w} \leftarrow \mathbf{M}\mathbf{u}_{j+1}$;
  $\mathbf{h} \leftarrow \mathbf{U}_{j+1}^T \mathbf{w}$;
  $\mathbf{f}_{j+1} \leftarrow \mathbf{w} - \mathbf{U}_{j+1}\mathbf{h}$;
  $\mathbf{H}_{j+1} \leftarrow (\hat{\mathbf{H}}_j, \mathbf{h})$;
end for

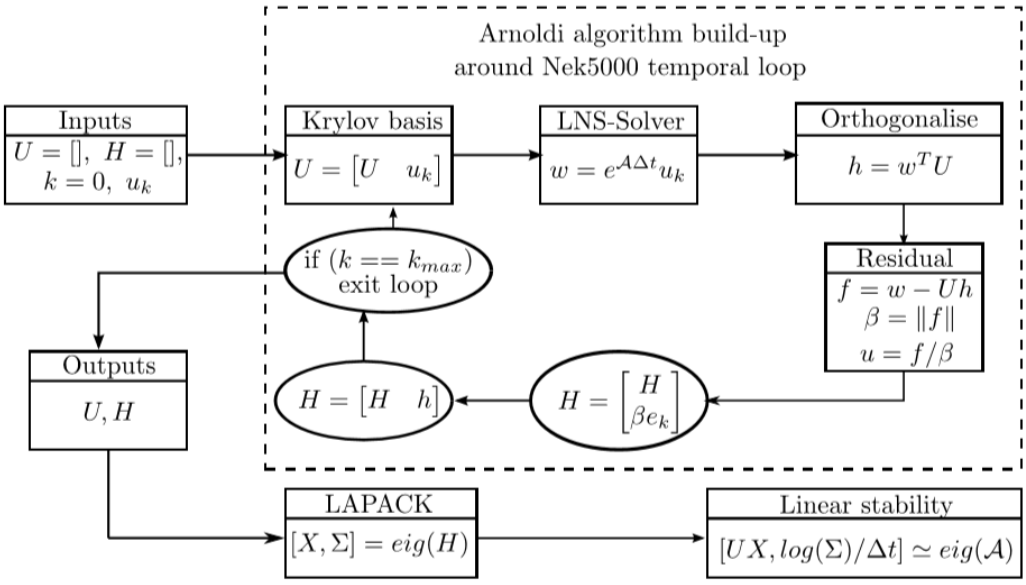

Figure 3.2: Block diagram of the time-stepping Arnoldi algorithm implemented around the Nek5000 temporal loop. Figure from Loiseau thesis [13].

Chapter 4

Linear stability analysis for flow around a square cylinder

In this chapter, we present numerical results concerning the stability analysis for flow past a 2D square cylinder. The first part of this chapter will be dedicated to the results of flow past a solid square cylinder and in the second part we will present the DNS and linear stability analysis for flow past a square cylinder covered by a porous layer. These results will be compared in order to enhance the influence of the porous coating on the flow dynamics. The flow regime at low Reynolds number ($Re \leq 60$) is investigated; in particular close to the **first bifurcation** occurring at $Re \simeq 45$.
To validate the current implementation, DNS computations have been performed for each case (solid square cylinder and porous square cylinder) to verify the flow behavior and characteristic quantities (such as the Strouhal number). Different steps of the stability analysis are then performed with the numerical tools presented in the previous section, starting with the computation of base flows. First of all, to introduce this chapter, we will recall some concepts about the **flow around bluff bodies**, such as the square or circular cylinder.

4.1 Literature survey on flow past a 2D square cylinder

It is helpful to recall some physical concepts about both the flow around the circular and the square cylinders, as significant similarities are shared. We will see how the flow behavior changes when the Reynolds number is increased. We know that the Reynolds number is the only parameter that prescribes the dynamics of the flow. Therefore, it is possible to classify the different dynamics of the flow as a function of the Reynolds number's evolution. The key difference between flow around a circular cylinder and a square cylinder is the threshold at which the flow behavior changes; this is due to the different shape of the solid obstacle and linked to the presence of discontinuities in the square cylinder corners. Furthermore, it is possible to verify in the literature that the critical Reynolds number for the square flow cylinder is more sensitive to the cross-domain size concerning the classical circular cylinder flow.

Four different behaviors are commonly identified (values from [10]):

1. **Laminar steady regime**: in this stable regime, the flow is steady, and a dually symmetrical recirculation bubble with respect to the centerline of the wake is formed; for the circular cylinder, this is obtained for $Re < 47$ while for the square for $Re < 46$.

2. **Laminar vortex shedding regime**: at parameter values above the critical Reynolds number, a Hopf bifurcation occurs, and a periodic shedding rises due to the von-Kármán mode; for the circular cylinder, this behavior takes place for $47 \leq Re < 190$ and in the range $46 \leq Re < 166$ for the square cylinder.

3. **Three-dimensional wake transition regime**: by further increasing the Reynolds number, a second bifurcation occurs and is characterized by the breaking of the spanwise symmetry; the 2D flow becomes 3D. The three-dimensional configuration is observed in the range $190 \leq Re < 270$ for the circular body and at $166 \leq Re < 210$ for the square.

4. **Wake transition to turbulence**: for values $Re > 270$ for the circular cylinder and at $Re > 210$ for the square, the flow becomes turbulent, and predictability becomes more uncertain as the control parameter is increased.

4.2 Numerical setup

A schematic view of the computational domain is shown in figure 4.1. It is known that the height of the domain H must be greater enough with respect to the square side length d so as not to introduce a fictitious acceleration in the flow. This effect can be measured by the **blockage ratio** defined as $\beta = d/H$; in the present work, $\beta \simeq 4.8\%$ is such that the flow behavior is unaltered.
The mesh was built with the open-source mesh generator Gmsh [9]; the employed mesh is composed of $N \simeq 30k$ elements, giving a good compromise between computational cost and accuracy. The number of the nodes on the surface of the square cylinder is 36. The mesh details are shown in figure 4.2, and it can be seen the mesh size is not uniform throughout the domain, being denser near the square cylinder and in the wake. In these zones, stronger velocity gradients are expected and a fine mesh is required in order to capture even the smallest flow scales. For all the simulations, the time step Δt is bounded by the CFL (Courant–Friedrichs–Lewy) defined as:

$$CFL = \frac{|u|\Delta t}{h} \tag{4.1}$$

with $|u|$ the magnitude of the velocity through an element and h the mesh size. The threshold for the stability condition of the numerical scheme is set to $CFL \leq 0.5$ and so the time step Δt is calculated to satisfy the condition.
Concerning the boundary conditions, at the inlet, a uniform velocity field $\mathbf{U}_\infty = (u_x, 0)$ is imposed whereas at the outlet a Neumann boundary condition is employed. On the top and bottom of the domain, a symmetric slip boundary condition is applied and on the cylinder surface, the no-slip boundary condition ($\mathbf{u} = \mathbf{0}$) is imposed. For this project, we choose a square side length $d = 1$ and the x-component of the free-stream velocity $u_x = 1$.

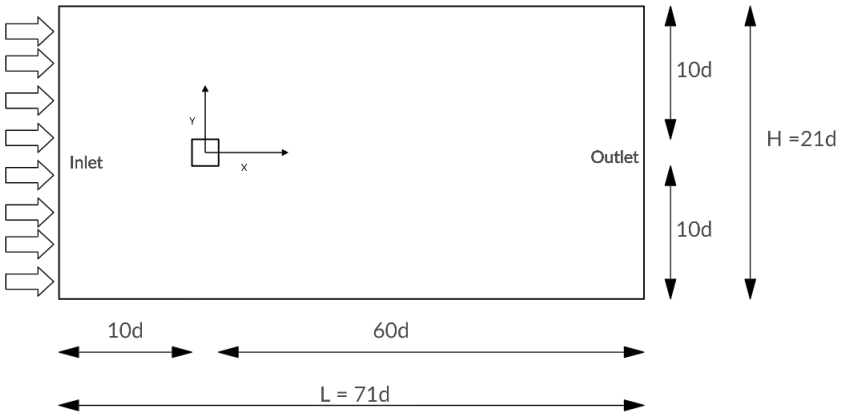

Figure 4.1: Schematic representation of the computational domain (not in scale).

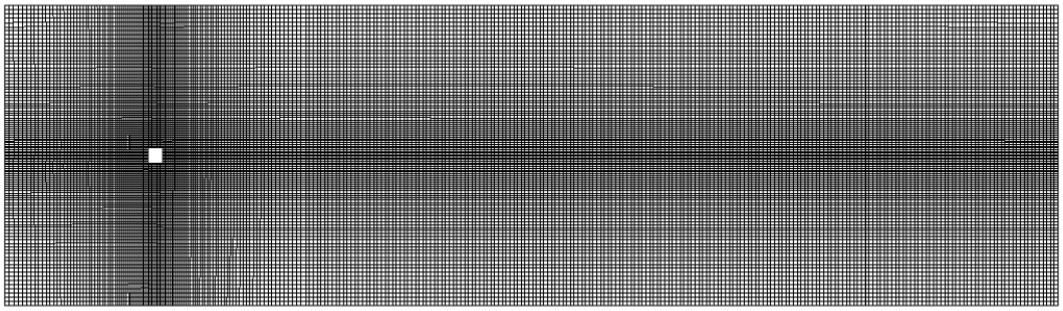

Figure 4.2: Mesh for the flow past a 2D square cylinder.

4.3 Numerical results for flow past a solid square cylinder

4.3.1 DNS computations

To check the flow behavior, we performed direct numerical simulations (DNS) at different Reynolds numbers and in particular, we focus on the **Strouhal number**. The Strouhal number is a dimensionless number that is defined as:

$$St = \frac{fd}{U} \tag{4.2}$$

where f is the **vortex shedding frequency**, d is the square length side and U is the characteristic flow velocity (in this work, U has been chosen like the freestream velocity U_∞). In CFD this number is very important because it describes the oscillating flow mechanisms. Since in this work $d = U = 1$, the Strouhal and the vortex shedding frequency are the same thing. Figure 4.3 shows the velocity field for different Reynolds numbers. The simulation has been performed for dimensionless time $t = 1000$. As we can see, the case at $Re = 43$ seems stable while the second one at $Re = 50$ seems unstable; we can check this behavior by looking at the evolution of the vertical velocity v in time. To do so, we use a probe that is placed in the middle of the wake, at the point $P = (20, 0)$. Remember that the origin of the reference system is placed in the center of the square cylinder.

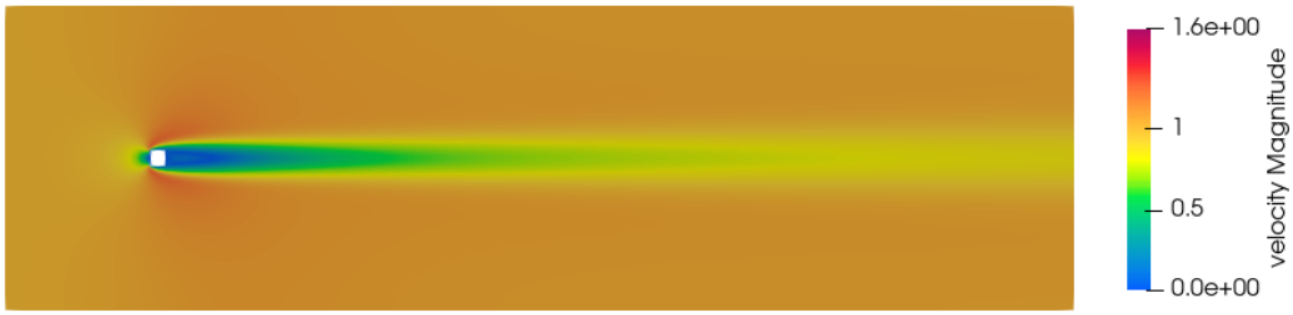

(a) $Re = 43$

(b) $Re = 50$

Figure 4.3: Instantaneous velocity magnitude for different Reynolds numbers.

From figure 4.4 we can make several observations. As stated above, the flow at $Re = 43$ is stable since we can see that the perturbation at the beginning grows in time but quickly decays exponentially in time. This is due to the viscous effects, that force the flow to the **stable fixed point**. We can also observe that the amplitude of the perburation is $\simeq 10^{-6}$ that basically means zero.
On the other hand, when the Reynolds number is set to $Re = 50$, the flow is unstable: the perturbation starts to grow around $t \simeq 300$ and reaches a limit cycle at $t \simeq 700$. This behavior is caused by the unstable mode, that in this case is the **Von Karman vortex street mode**, which deforms the base flow. The vortex shedding is observed in figure 4.5 which shows the time evolution of the streamlines for $Re = 50$. Now, we check the frequency at which the flow oscillates through a PSD (Power Spectral Density). The spectrum of the whole signal in shown in figure 4.6. The frequency we are interested in coincides with the peak of the spectrum, which is approximately $f \simeq 0.1162$. This is in good agreement with the literature [10]. An interesting thing is that the spectrum is composed only by **odd harmonics**; in fact, we have the first and the third harmonics, respectively, $f_1 \simeq 0,1162$ and $f_3 \simeq 0,3486$. This symmetry of the flow is due to the shape of the cylinder: when we have a circular cylinder, the spectrum is composed by odd and even harmonics while for the square cylinder the even harmonics are suppressed.
The vortex shedding frequency (or the Strouhal number) calculated is also verified by the **Roshko formula** [19], a well known relationship used in fluid dynamics that links the Reynolds number to the Strouhal one. The formula proposed by Roshko is the following:

$$St = A + \frac{B}{Re} \tag{4.3}$$

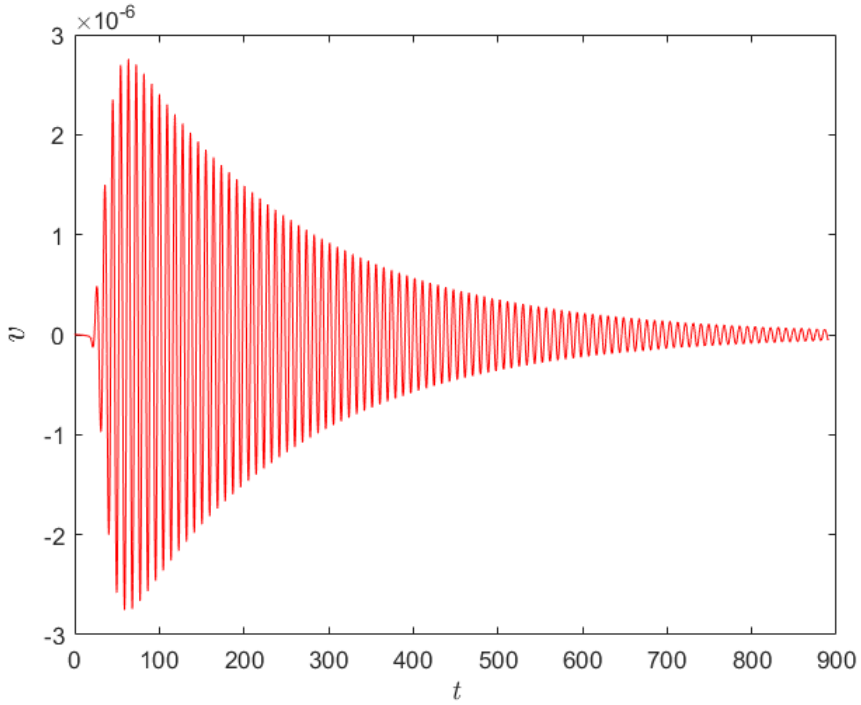

(a) *Re = 43*

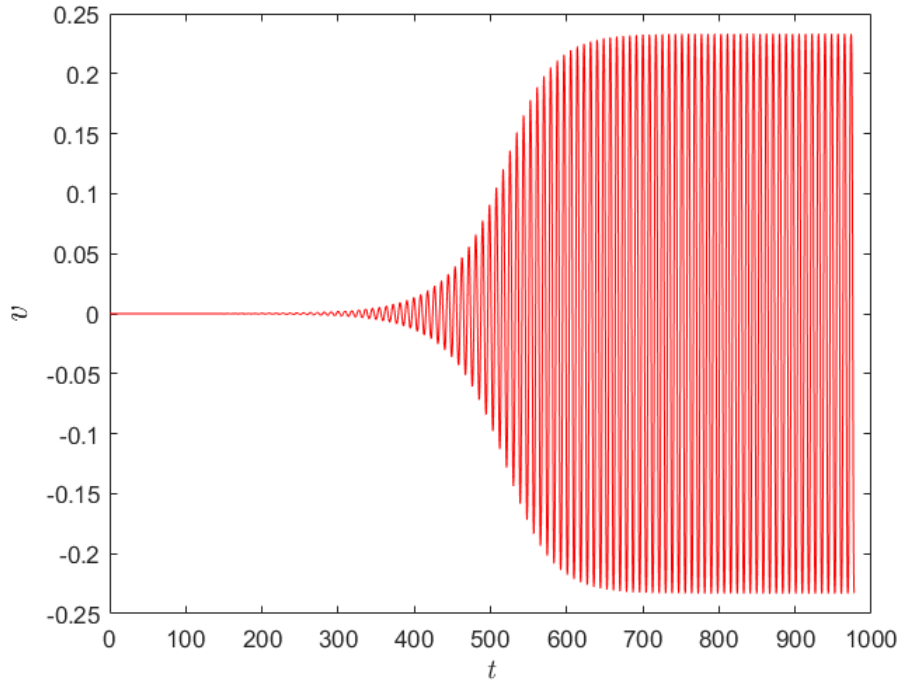

(b) *Re = 50*

Figure 4.4: Vertical velocity over time for different Reynolds numbers.

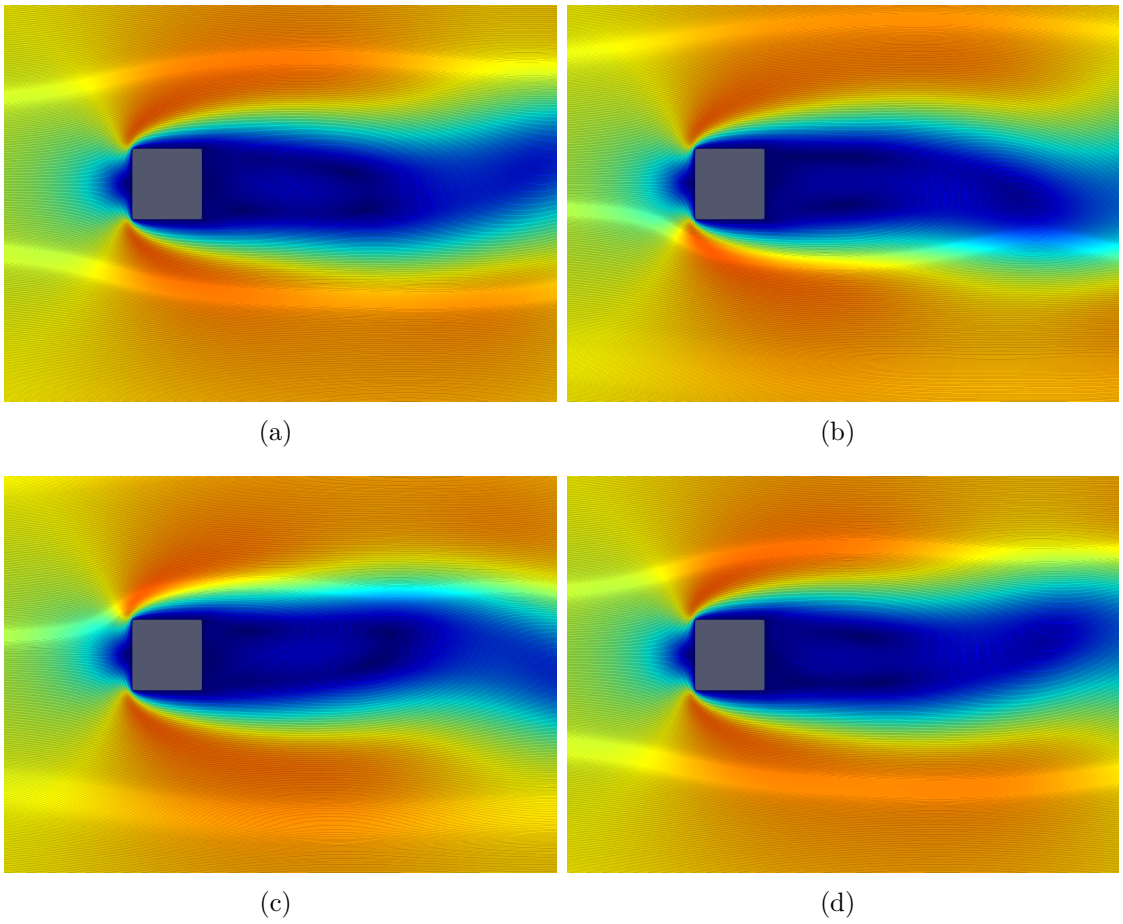

(a) (b)

(c) (d)

Figure 4.5: Streamlines: (a) t=992, (b) t=994, (c) t=996, (d)t =999 for $Re = 50$.

where $A = 0,2175$ and $B = -5,106$ for the circular cylinder. In figure 4.7 are shown the present DNS results for square cylinder against Roshko for circular cylinder.

4.3.2 Linear stability analysis

Now the code is validated, linear stability analysis is performed. This analysis consists in two steps:

1. calculate the **fixed points** of the system with the selective frequency damping method;

2. solve the **eigenvalues problem** with the Arnoldi algorithm to characterize the stability of the fixed points.

The SFD method works by damping the most unstable frequencies linked to hydrodnamic instabilities. Then is important to understand that we need to use the SFD method only when the Reynolds number is **supercritical** Reynolds numbers, i.e. $Re > Re_c$, because in this case the flow oscillates with the vortex shedding frequency and we want to kill it to compute the fixed points. When the Reynolds number is **subcritical**, i.e., $Re < Re_c$ we don't employ the SFD method because the flow doesn't oscillate; in this case, DNS computation and SFD computation give us the same results. Figure 4.8 depicts an example of base flow computation at $Re = 50$.

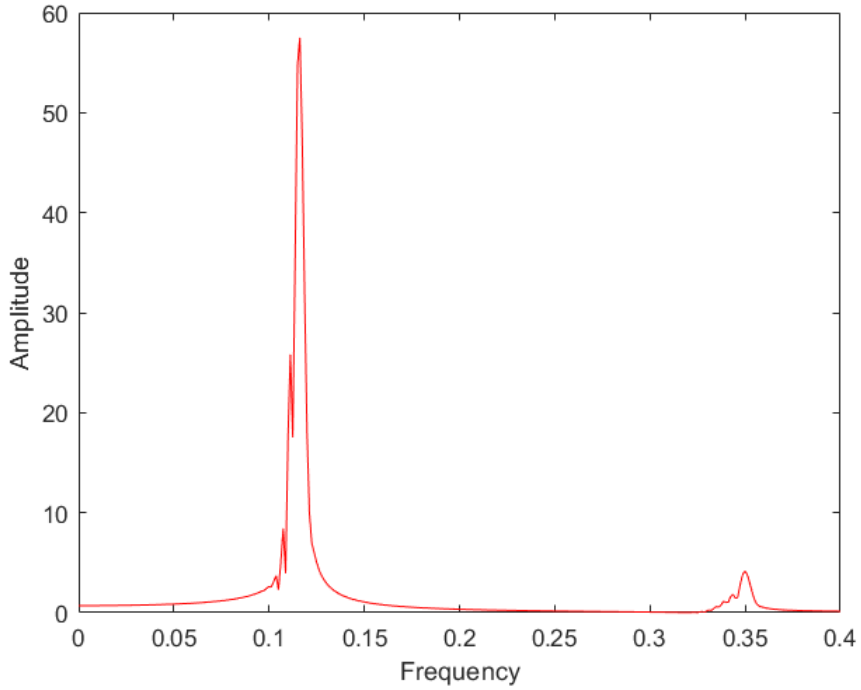

Figure 4.6: Signal spectrum for the case $Re = 50$.

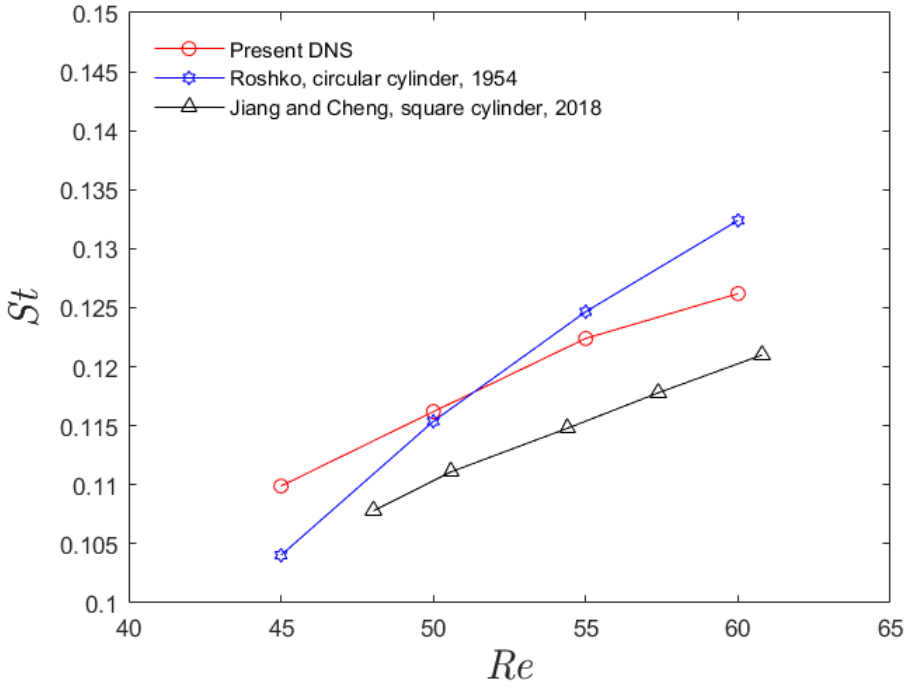

Figure 4.7: Strouhal number St versus Reynolds number Re.

Throughout this work, it has been considered that the solution reaches the steady-state when the residual $R = ||\mathbf{u}_{n+1} - \mathbf{u}_n||/\Delta t$ converges down to $R \simeq 10^{-9}$. To see the influence of the cut-off frequency ω_c and of the gain χ on the residual R many simulations have been performed. Figure 4.9 shows these results. Furthermore, fig-

(a) DNS computation for Reynolds number $Re = 50$.

(b) Base flow computation for Reynolds number $Re = 50$.

Figure 4.8: Velocity field versus unstable equilibrium.

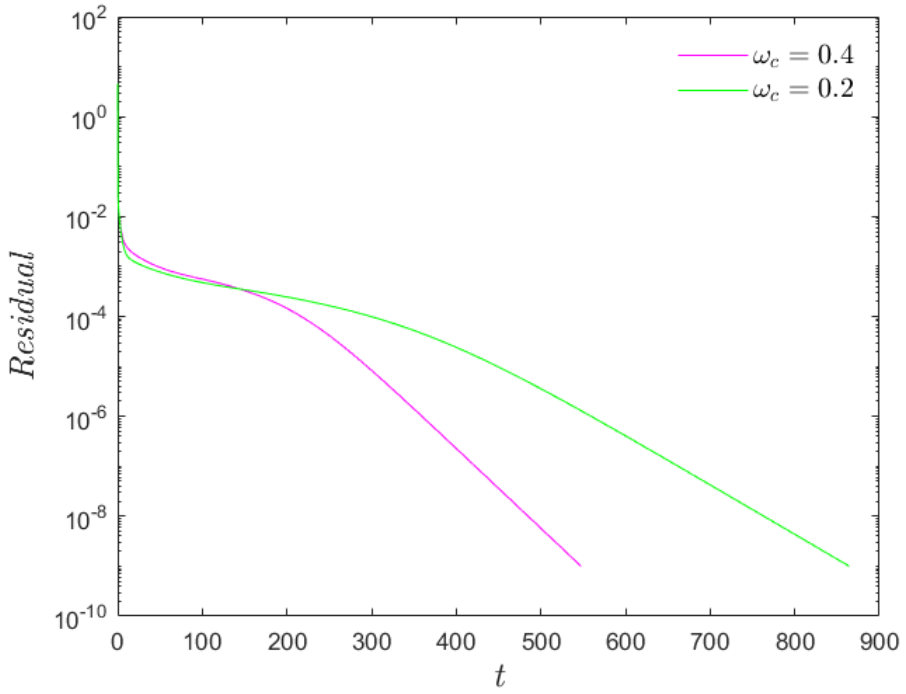

Figure 4.9: Time evolution associated to the residual R needed to reach a steady state converged down to $R \leq 10^{-9}$. $\chi = 0.2$

ure 4.10 gives the recirculation lengths obtained through the isocontour $u = 0$ of the x-velocity from the base flow at different Reynolds numbers. Even if this physical quantity is generally deduced from the mean flow, it is important to notice that

the **linear trend** is respected. Running a DNS simulation from the base flow is

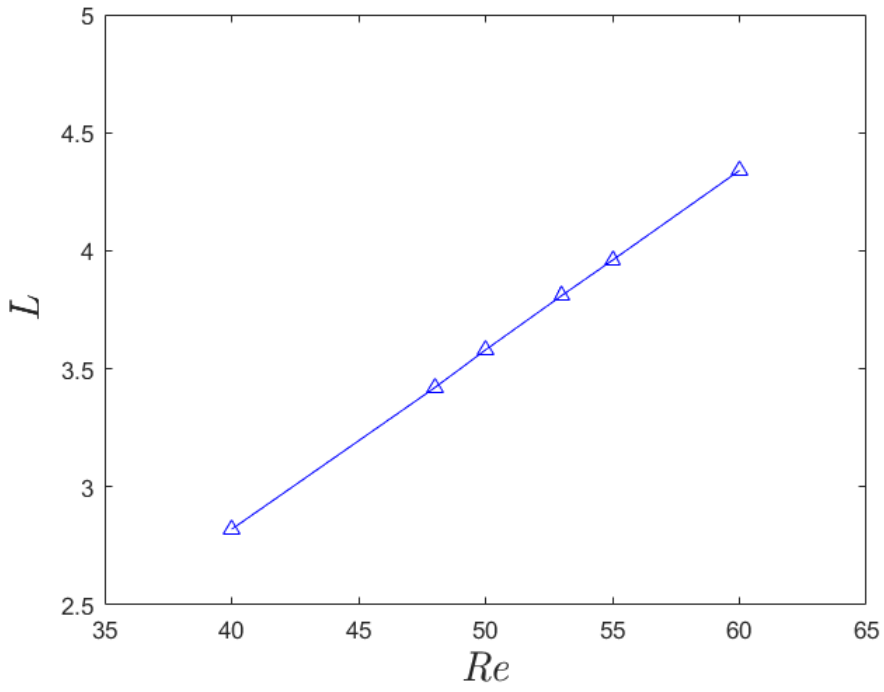

Figure 4.10: Recirculation length against Reynolds number.

possible to track different interesting graphics that are useful for understanding the physics of our dynamical system. First, let us consider figure 4.11 which represents a semi-log plot of the vertical velocity over time. As we can see, at the beginning the perturbation grows linearly over time and then the perturbation reaches a **non-linear saturation**, i.e the limit cycle. The slope of the linear tract is precisely the growth rate of the instability σ; in fact, we remember that the perturbation for our study is in the form of normal modes:

$$v' = v_0 e^{\psi t} = v_0 e^{\sigma t} e^{i\omega t} \tag{4.4}$$

where σ is the growth rate of the instability whereas ω is the eigenfrequency. So if we take the log of the previous equation and consider only the real part, we obtain:

$$\Re\Big[\log\Big(\frac{v'}{v_0}\Big)\Big] = \sigma t. \tag{4.5}$$

Of course, equation 4.5 is only valid in the linear tract. What happens is that, initially, the perturbation evolves linearly over time, in agreement with our linear study but at some point, the non-linear effects become preponderant and so, in this regime the flow is non-linearly saturated. Through Figure 4.14 is possible to understand the importance of the non-linear effects; in fact, it shows the difference that exists between the frequency obtained from the DNS and the one as a result of the stability analysis. What we expect is that when the Reynolds number is close to the critical one, the two frequencies are approximately the same. On the other hand, is clear that when the Reynolds number increases, the non-linear effects become more important and so the difference between the two frequencies grows.

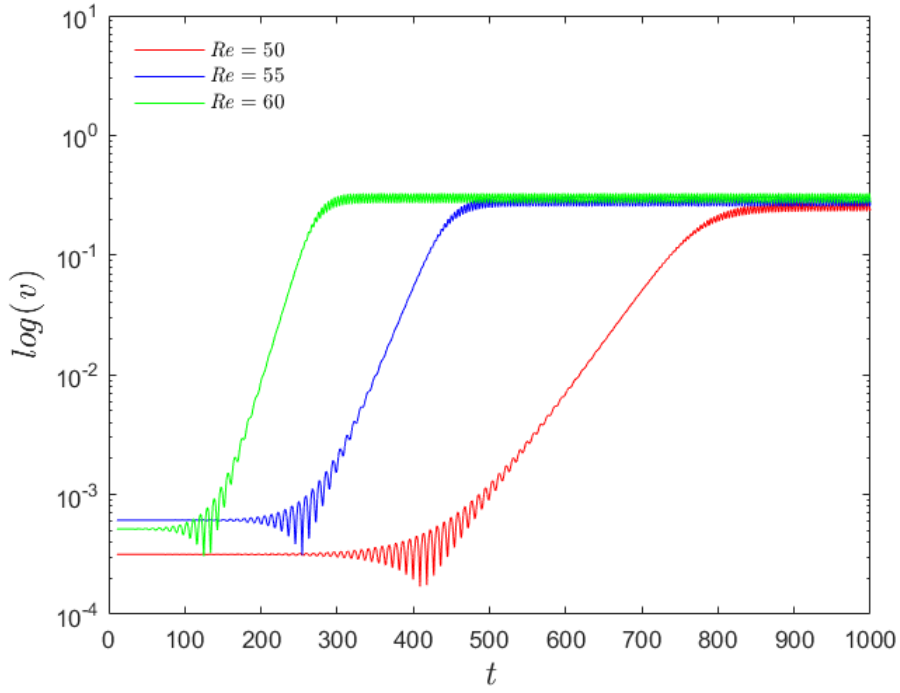

Figure 4.11: Semi-log plot of the vertical velocity over time for different Reynolds numbers.

Finally, figure 4.12 and 4.13 give the phase plots, i.e. the vertical velocity against his first (4.12) or second (4.13) time derivative. In particular, figure 4.12 is exactly the Hopf bifurcation in his **canonical form**. We can see that for both cases when increasing the Reynolds number the non-linear distortion becomes more important. The last step of this part is solving the eigenvalues problem to characterize the stability of the baseflow. Many simulations have been performed to carry out the eigenspectra and the eigenfunctions. For all the simulations, it has been set a Krylov subspace dimension $k = 250$ and a residual $R = 10^{-6}$. To begin let's consider the linear stability of the flow around the square with $Re = 50$; the corresponding eigenspectrum is shown in figure 4.15 and as we expected, this configuration is unstable since it's leading eigenvalue has real part greater than zero ($\sigma > 0$). Figure 4.18 shows the real part of the eigenfunctions associated with the leading eingevalue.

To find the **critical Reynolds number**, we can do a linear interpolation; to do this, we need two cases where the growth rate σ is close to zero, i.e. $\sigma \simeq 0$. Linear stability computation show us that these two cases are for $Re = 43$ and $Re = 45$, as we can see in the figure 4.16. Through the linear interpolation we find a critical Reynolds number $Re_c \simeq 44$, as can be seen on figure 4.17 which traces the neutral curve that shows that show the growth rate σ against the Reynolds number Re. This curve is compared with the results proposed by Kelkar et al. [12] where they found a critical Reynolds number $Re_c \simeq 53$. This difference should be due to the blockage ratio and mesh size. Then to view how the critical value is affected by the blockage ratio it would be necessary to perform another study with different mesh. What we should expect by varying the blockage ratio is only a shift of the threshold for the critical Reynolds number. Of course, we expect the same flow behavior and physics.

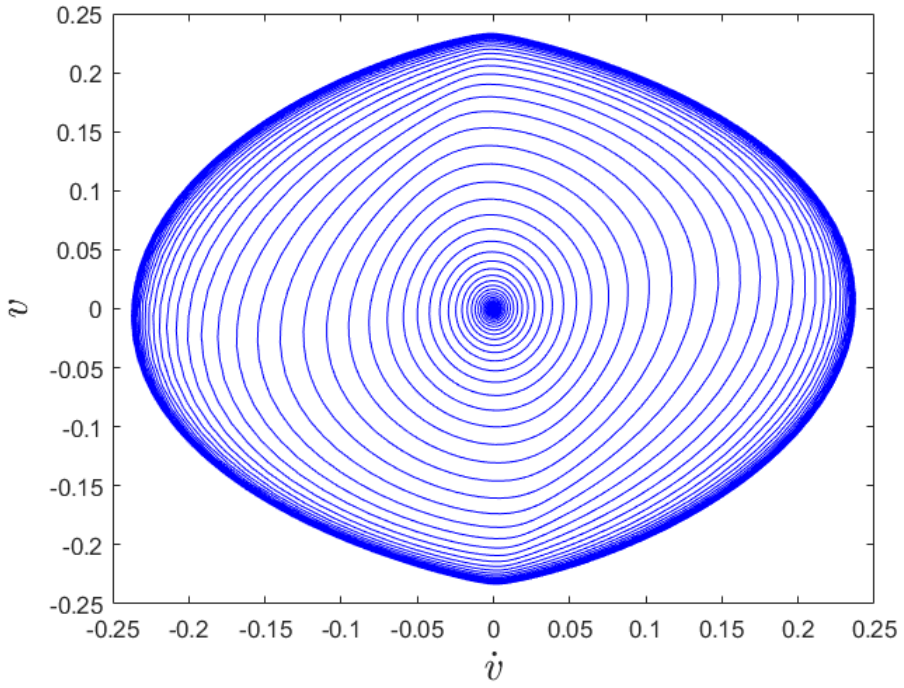

(a)

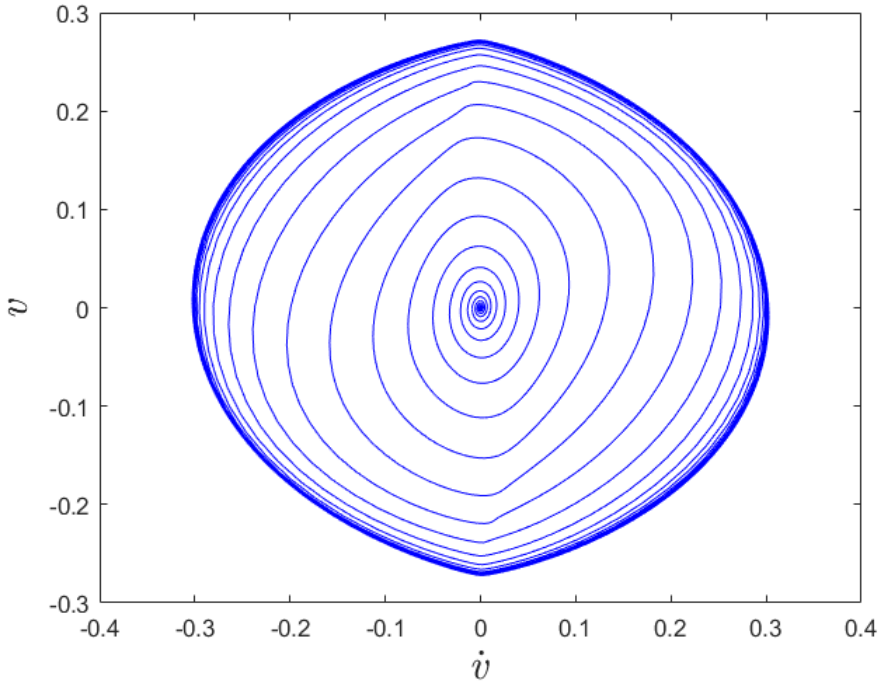

(b)

Figure 4.12: Phase plot $(v, \dot{v})$ for flow past a square cylinder: (a) $Re = 50, (b) Re = 60$.

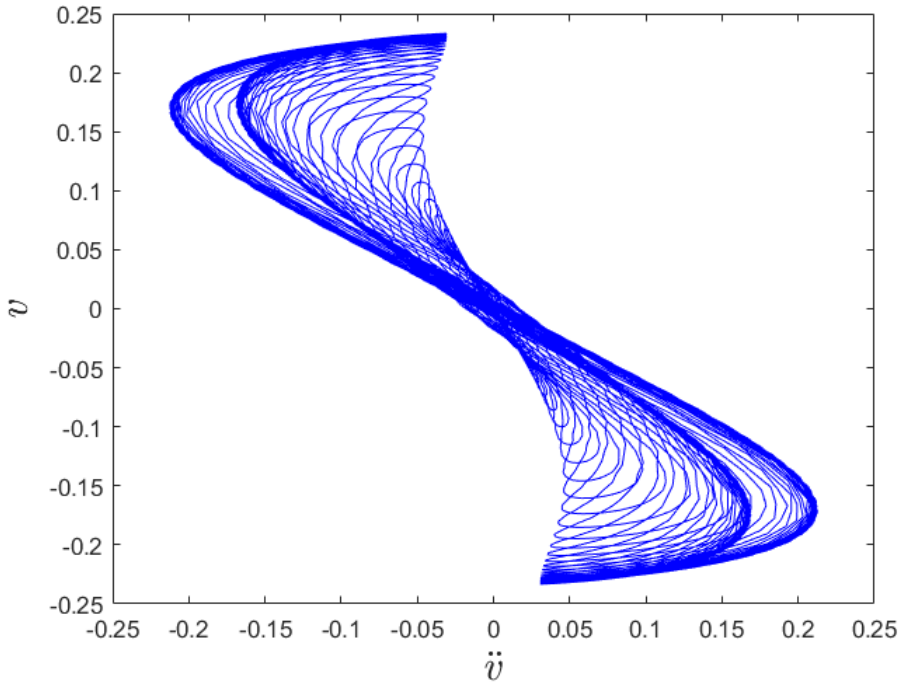

(a)

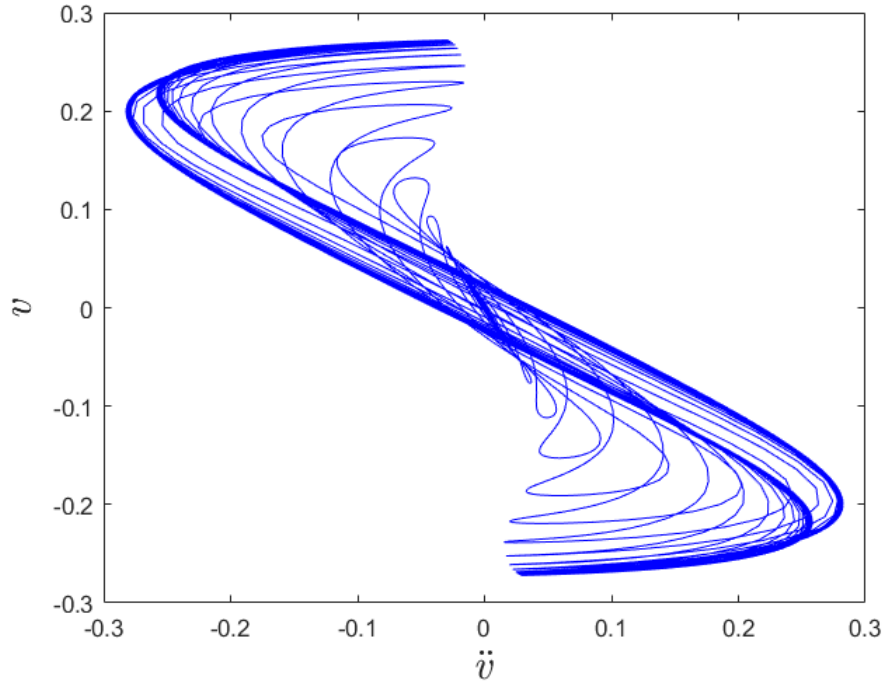

(b)

Figure 4.13: Phase plot $(v, \ddot{v})$ for flow past a square cylinder: (a) $Re = 50, (b) Re = 60$.

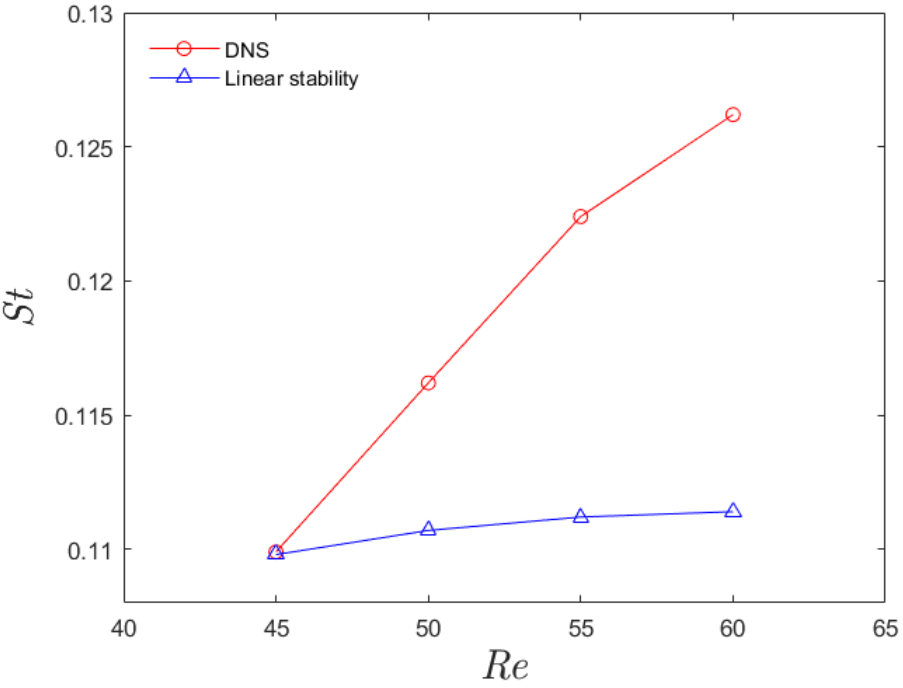

Figure 4.14: Non-dimensional frequency against the Reynolds number.

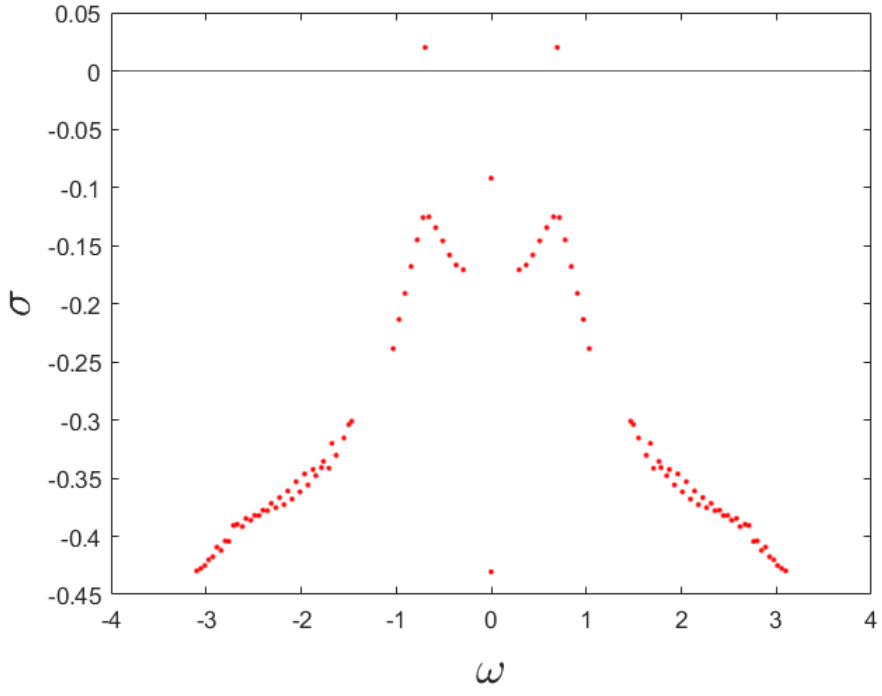

Figure 4.15: Eigenspectrum for the flow past a solid square cylinder at $Re = 50$.

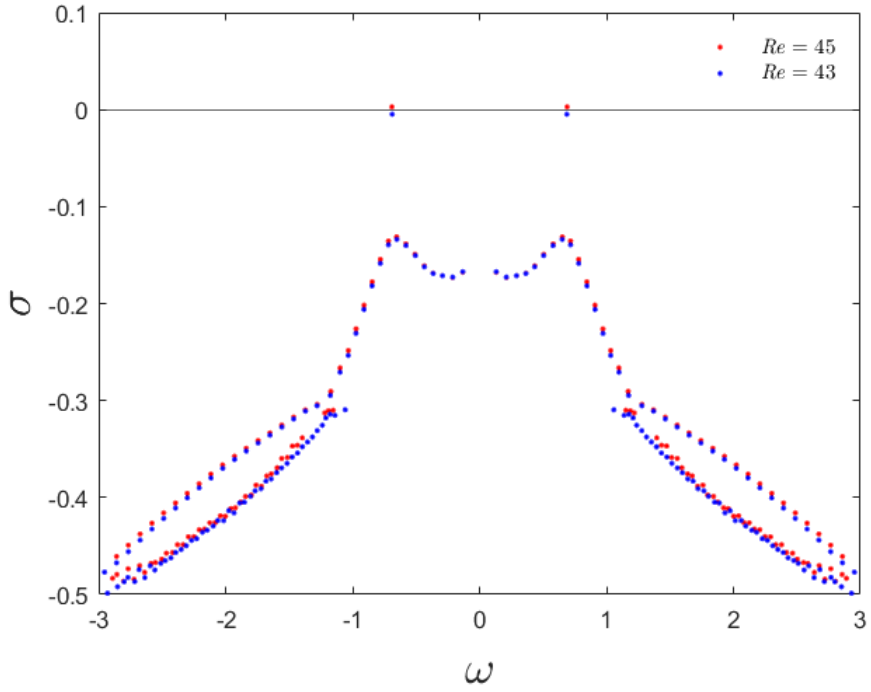

Figure 4.16: Eigenspectra for the flow past a solid square cylinder at $Re = 43$ and $Re = 45$.

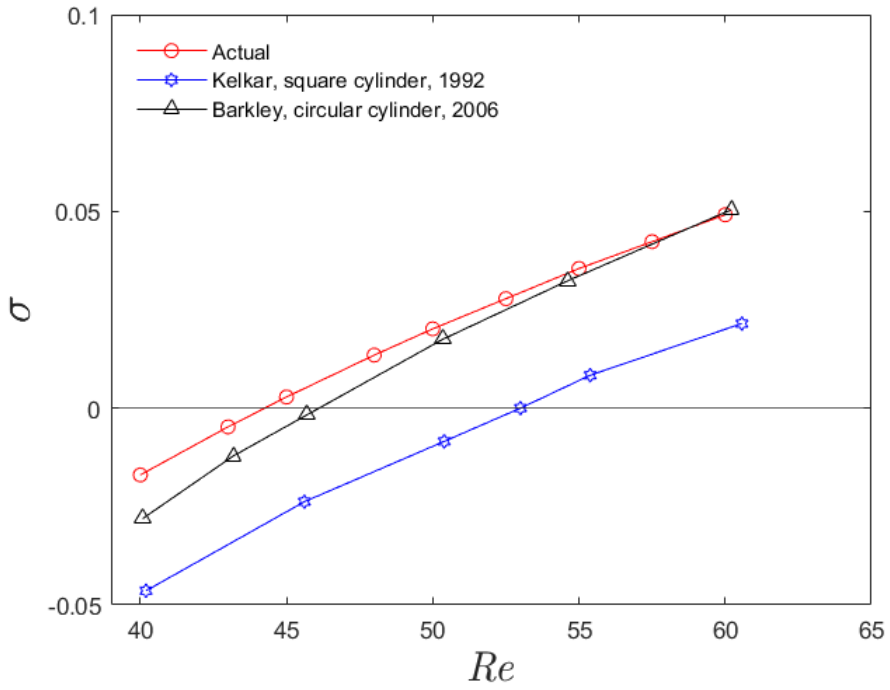

Figure 4.17: Growth rate of the instability σ against Reynolds number Re for the flow past a solid square cylinder.

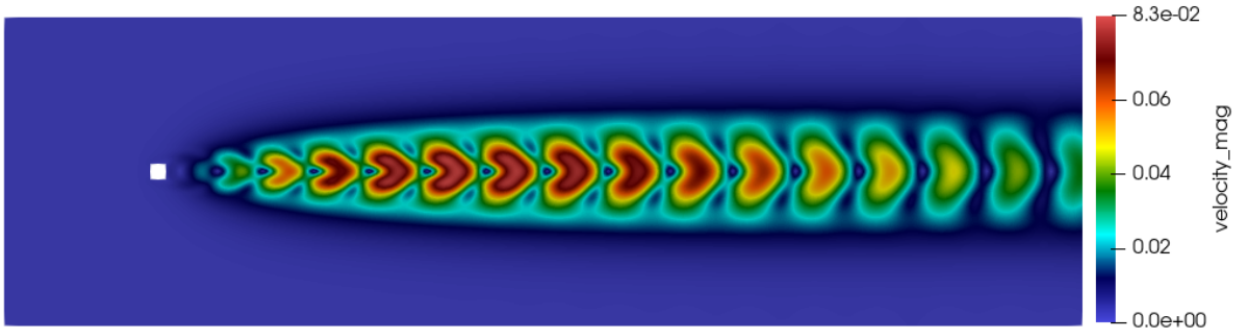

(a) Velocity magnitude **u**.

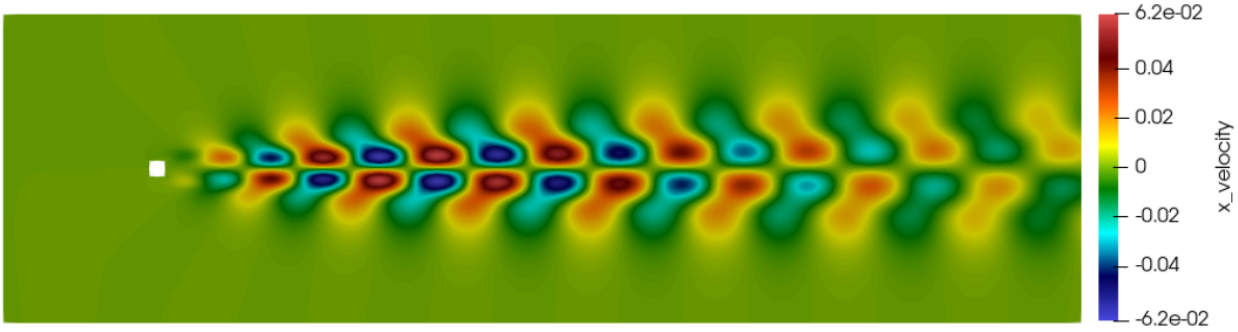

(b) Streamwise component of the velocity (u).

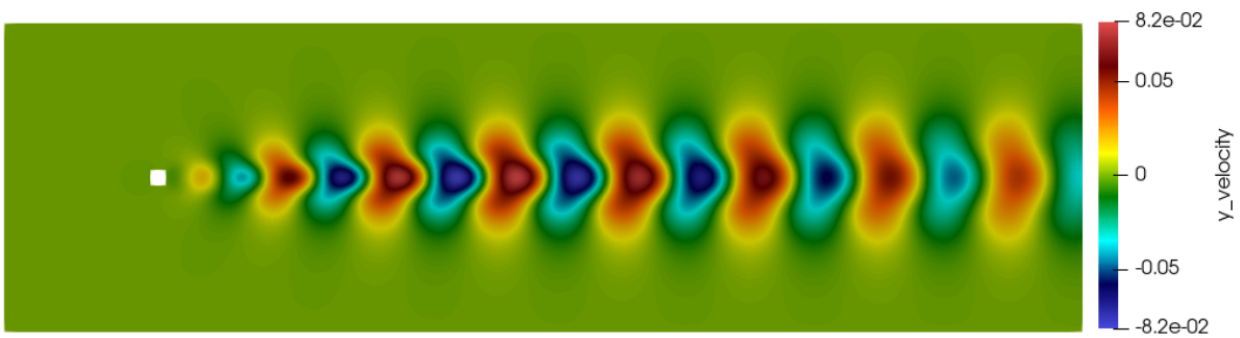

(c) Vertical component of the velocity (v).

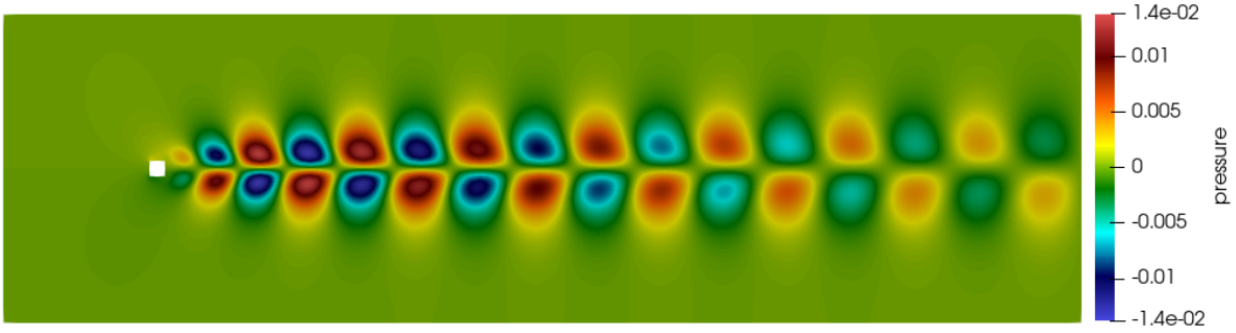

(d) Pressure p.

Figure 4.18: Real part of the globally unstable modes associated with leading eigenvalue for the flow past a solid square cylinder at $Re = 50$.

4.4 Numerical results for flow past a porous square cylinder

This part is the core of the present study in which we will investigate how the flow past an obstacle is modified due to the presence of a porous layer around it. Now, we consider a solid square cylinder surrounded by an homogeneous porous layer of uniform permeability, porosity and thickness. In order to have the total diameter of the square always equal to one, $d_{cube} = 1$, we need to reduce the diameter of the square for taking into account the porous layer. We set the diameter of the solid obstacle to $d_{solid} = 0.8$ and the thickness of the porous layer to $s = 0.1$ in order to have $d_{cube} = d_{solid} + 2s = 1$. We recall that the square cylinder is located at $(x, y) = (0, 0)$ in the computational domain $D = [-10, 60] \times [-10, 10]$ and the time step at each iteration is bounded with the CFL condition in order to have the $CFL \simeq 0.5$. Each DNS simulation is performed for dimensionless time $t = 1000$.
Since the purpose of the porous layer is to control the flow, we expect a delay in the flow regime transition, that is to say an increase of the critical Reynolds number.

4.4.1 DNS computations and validation

In order to validate the implementation of the Brinkman penalization model within the Nek5000 code, my simulation results of flow around a solid-porous obstacle have been compared to the numerical results issued from another code, called Hysop (Hybrid Simulations using Particles), which also uses the Brinkman penalization model and has already been validated in the context of porous flows, [16], [17]. In this code, the Brinkman Navier-Stokes equations are resolved in their dimensionless velocity($\mathbf{u}$)-vorticity($\boldsymbol{\omega}$) formulation, obtained by taking the curl of the Navier-Stokes equations:

$$\begin{cases} \dfrac{\partial \boldsymbol{\omega}}{\partial t} + \big(\mathbf{u} \cdot \nabla\big)\boldsymbol{\omega} = \big(\boldsymbol{\omega} \cdot \nabla\big)\mathbf{u} + \dfrac{1}{Re}\Delta\boldsymbol{\omega} - \nabla \times \Big(\lambda \chi_b \mathbf{u}\Big) \\ \Delta\mathbf{u} = -\nabla \times \boldsymbol{\omega} \end{cases} \tag{4.6}$$

where the vorticity is defined as $\boldsymbol{\omega} = \nabla \times \mathbf{u}$. In Hysop code, equations 4.6 are discretized using a numerical method called the "remeshed Vortex method". It is a semi-Lagrangian method (partially Lagrangian and partially Eulerian) which is based on the following splitting algorithm

1. the advection term is solved in a **Lagrangian way**, using particles. Once the particles have been advected at the fluid velocity, they are resmeshed on an underlying Cartesian grid.

2. once the particles are on the grid, one uses **Eulerian grid based methods** (FFT based or Finite-Differences methods) to solve all the other terms : the diffusion term, the stretching term (only in 3D), and the Brinkmann penalization term.

To know more details about the Vortex penalization method, you can refer to [16] and [17].
In this work, the whole control study using porous media will be performed at $Re = 60$. For the first validation step, we consider the two limit cases of flow past

a solid square cylinder with $d = 1$ and then with $d = 0.8$ (square cylinder without porous layer). For the configuration $d = 0.8$, what we expect is an increase of the Strouhal number respect to the flow with $d = 1$. This is a known result in the literature. Figure 4.19 shows the present results with Nek5000 for the two limit cases. Starting from the solid case with $d = 0.8$, what we should obtain is that

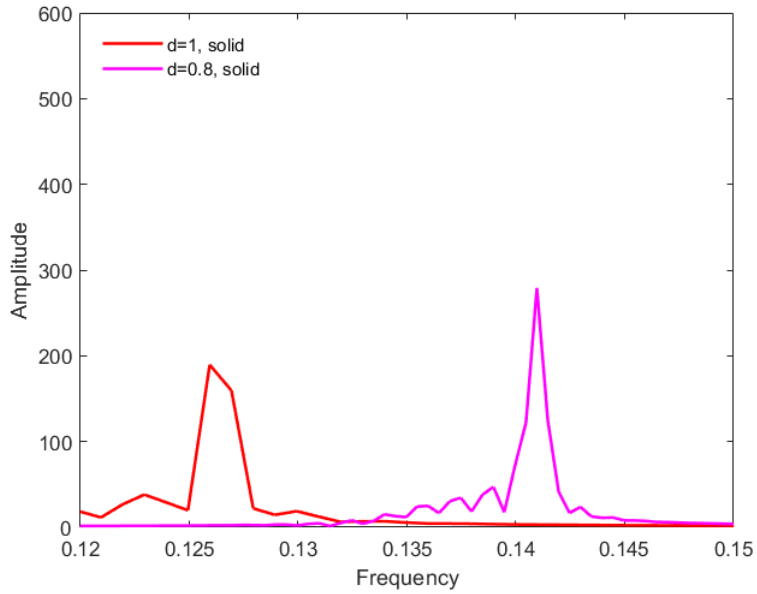

Figure 4.19: Signal spectrum for the two limit cases at $Re = 60$ (present results).

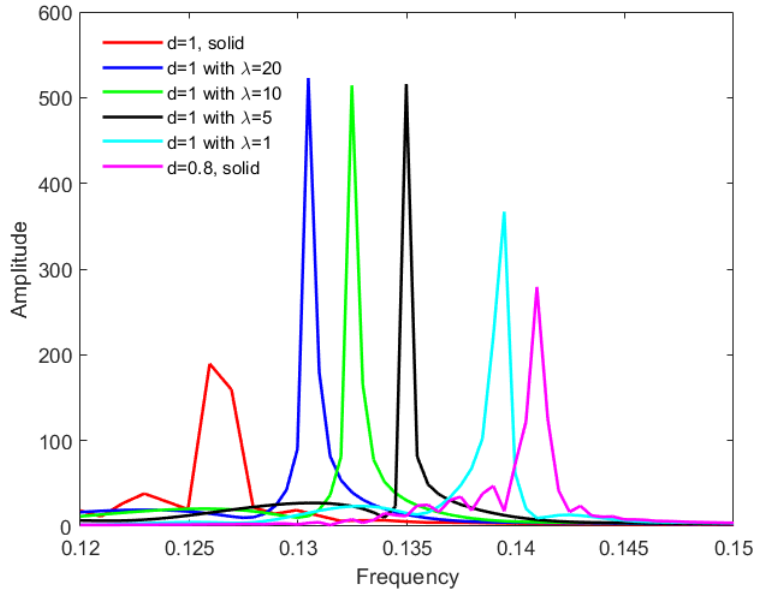

Figure 4.20: Signal spectrum for different control cases at $Re = 60$ (present results).

increasing the value of the λ parameter (i.e. decreasing the permeability) in the porous layer, would asymptotically tend to the solid case with $d = 1$. Figure 4.20 shows that this is actually what we obtain in Nek5000, since the porous cases with

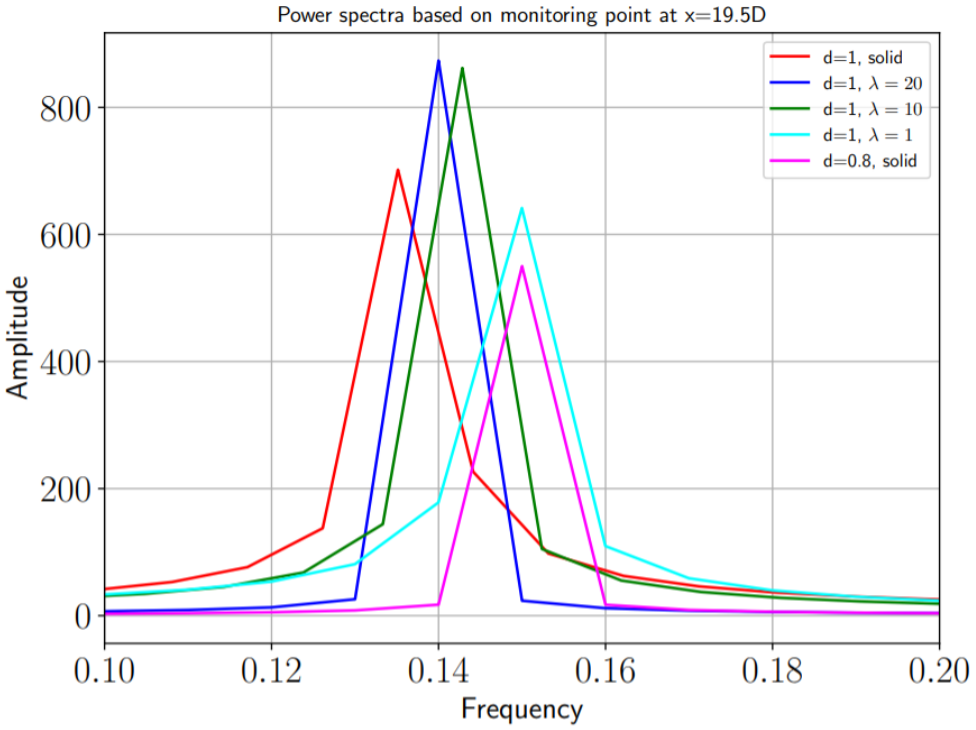

Figure 4.21: Signal spectrum for different control cases at $Re = 60$ (Hysop results).

$\lambda = 1, 5, 10$ and 20 are between the two limit solid cases.

This behavior is confirmed by the results obtained with Hysop code as shown in

Case	Present (Nek5000)	Reference(Hysop)
$d = 1.0$, solid	0.1259	0.1351
$d = 1.0, \lambda = 20$	0.1305	0.1400
$d = 1.0, \lambda = 10$	0.1325	0.1428
$d = 1.0, \lambda = 1$	0.1395	0.1498
$d = 0.8$, solid	0.1410	0.1500

Table 4.1: Comparison of Strouhal number values of the present work and reference.

figure 4.21 and table 4.1, which respectively report the power sectrum and numerical values of Strouhal number for each case. It has to be mentionned that the results obtained with Hysop derive from simulations performed in a smaller domain ($D = [-4, 21.6] \times [-5.12, 5.12]$) with a coarser resolution (25 grid points along the whole obstacle), which explains the quantitative dicrepancy between the results. However, what is important is that the tendency concerning the evolution of Strouhal number depending on λ is the same for both, i.e:

$$S_t(d = 1) > S_t(\lambda = 20) > S_t(\lambda = 10) > S_t(\lambda = 1) > S_t(d = 0.8) \qquad (4.7)$$

As another comparative quantity for the validation has been considered the y-profile of the mean streamwise velocity u_x at $x = 0$. Figure 4.22 shows the profile obtained with Nek5000 code whereas figure 4.23 the one obtained with Hysop code. What can be seen from figures 4.24 and 4.25 is that the trend of all curves is almost the same for both codes and so they are in good agreement. In order to be

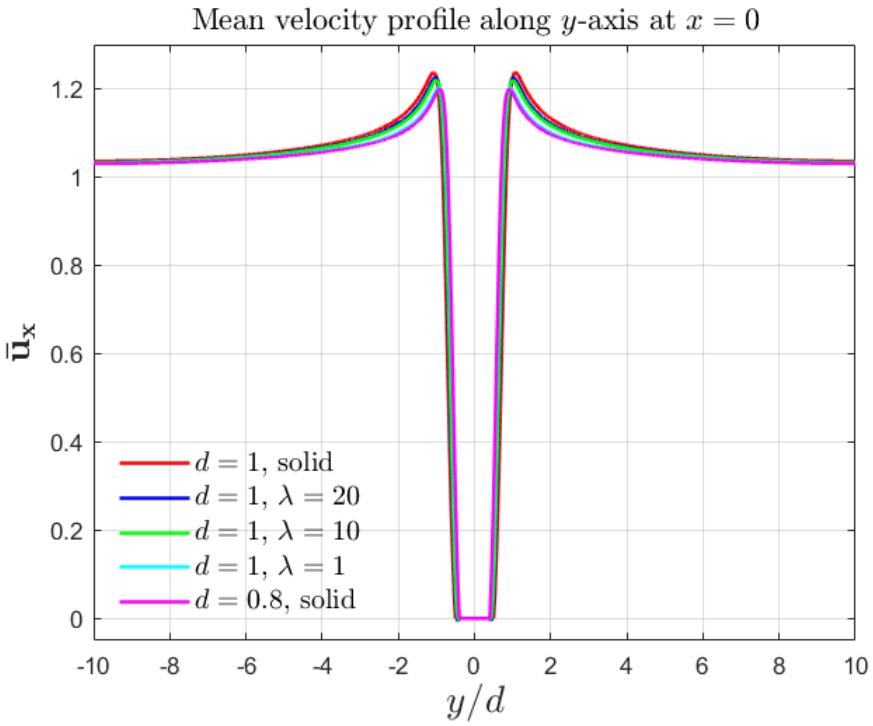

Figure 4.22: y-profile of the mean streamwise velocity u_x at $x = 0$. (present results).

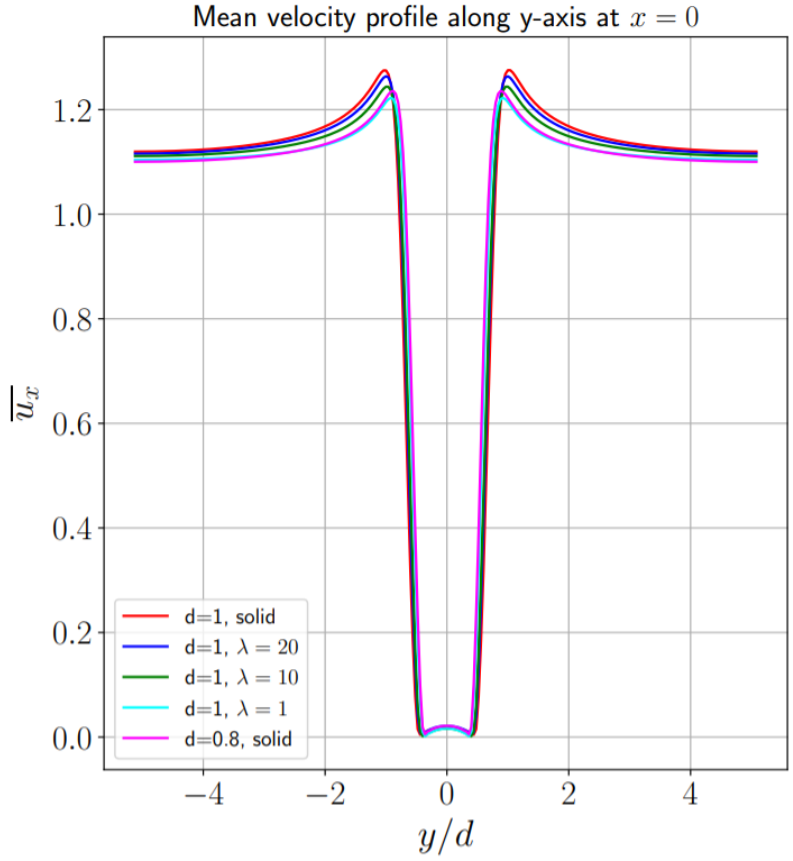

Figure 4.23: y-profile of the mean streamwise velocity u_x at $x = 0$. (Hysop results).

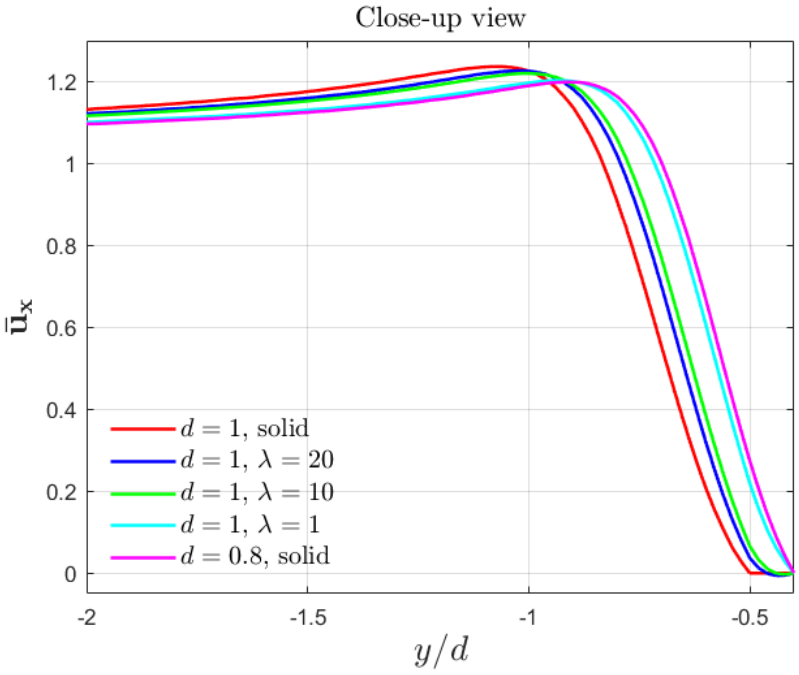

Figure 4.24: Close-up view of the y-profile of the mean streamwise velocity u_x at $x = 0$. (present results).

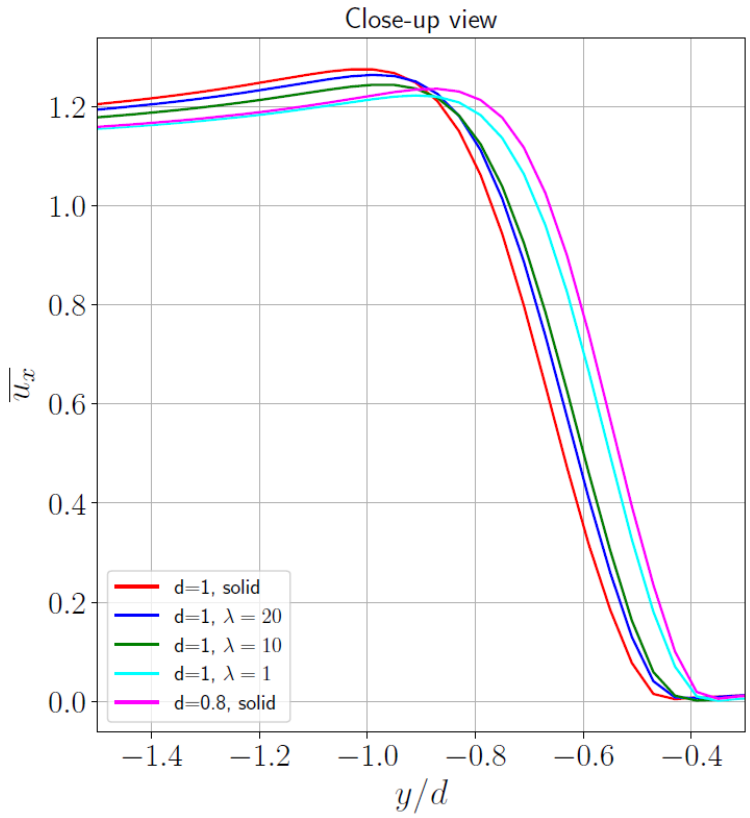

Figure 4.25: Close-up view of the y-profile of the mean streamwise velocity u_x at $x = 0$. (Hysop results).

fully confident in our present results with respect to the reference code Hysop, a simulation of the solid case with $d = 1$ (uncontrolled case) and of the porous case with $\lambda = 10$ (controlled case) have been performed in Nek5000 and in Hysop using a similar computational domain and a similar resolution; in Nek5000 the domain size and the mesh remain the same as presented before and in Hysop the 2 simulations are now performed in a domain $D = [-10, 30] \times [-10, 10]$ with 32 grid points along the whole obstacle. The results between the two codes are compared in terms of Strouhal numbers and of mean velocity profile of the streamwise velocity u_x along y-axis at $x = 0$. The Strouhal number is compared for the solid case $d = 1$ and for the porous one at $\lambda = 10$. Table 4.2 shows these values. What we can see is that the results obtained for both are in good agreement because for both cases we have a relative error $\varepsilon < 1\%$. The mean velocity profile is compared only for the solid case $d = 1$. Figure 4.26 shows this comparison. Also in the case, the results for both are very similar.

Case	Present (Nek5000)	Reference(Hysop)
$d = 1.0$, solid	0.1259	0.125
$d = 1.0, \lambda = 10$	0.1325	0.1315

Table 4.2: Comparison of Strouhal number values of the present work and reference.

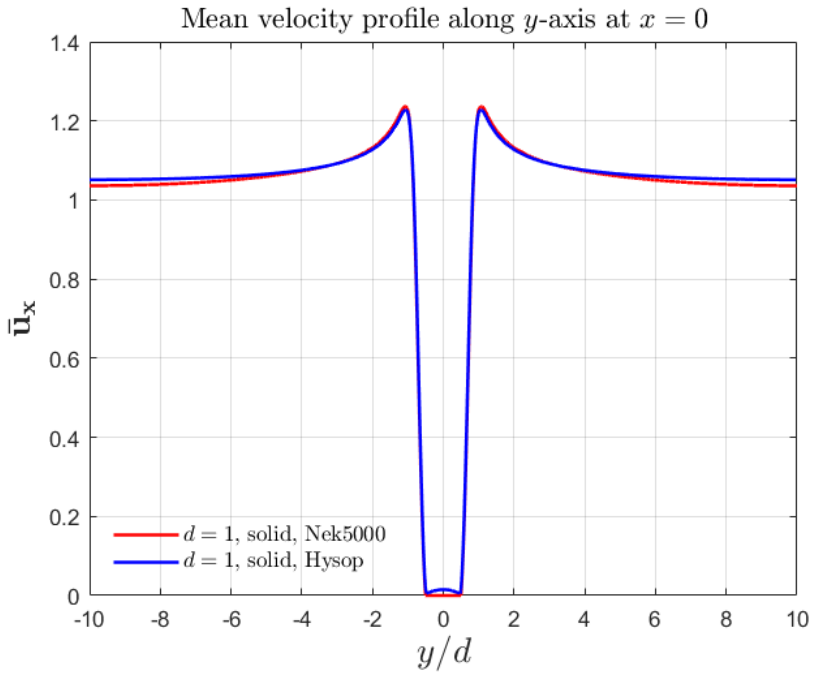

Figure 4.26: Comparison of the y-profile of the mean streamwise velocity u_x along y-axis at $x = 0$ for the flow past a solid square cylinder.

4.4.2 Linear stability analysis

As in the previous section, the linear stability is composed of two steps: base flow computation and resolution of the eigenproblem. The simulation parameters to find the base flow are always the same: $\chi = 0.2$ and $\omega = 0.4$. Corncerning the Arnoldi algorithm one sets a Krylov subspace dimension $k = 250$ and a theshold for the residual $R = 10^{-6}$. The principal purpose of this section is to see how the neutral curve is affected by the porous layer. We would like to answer the question "Does the increase of the dimensionless parameter λ inside the porous layer stabilize or destabilize the flow ?"
The neutral curve for this study is shown in the figure 4.27 for $\lambda = 10$ and $\lambda = 20$ and for the solid case with $d = 1$ ($\lambda = 0$). What we can observe is that, with the

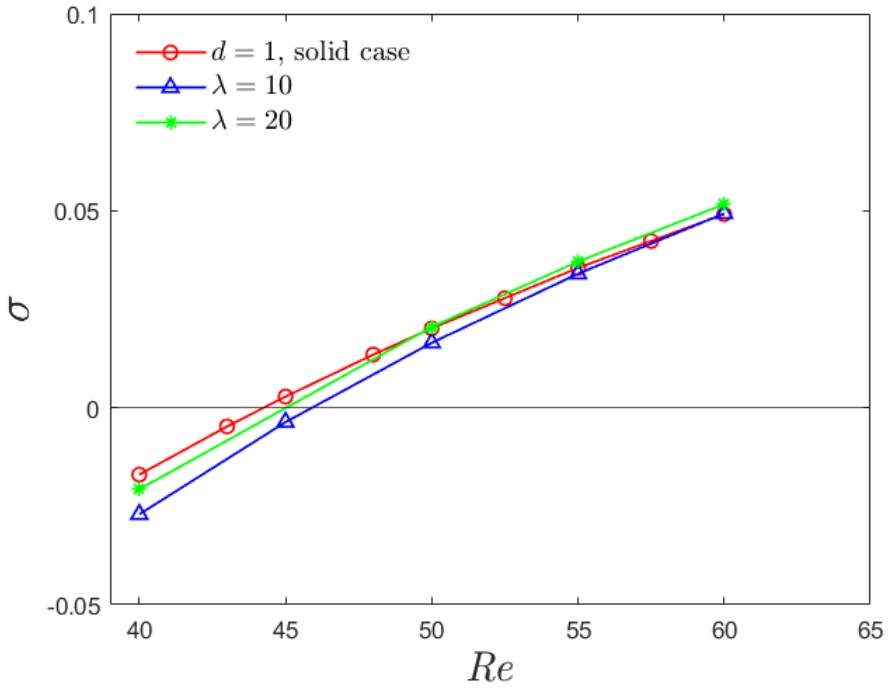

Figure 4.27: Neutral curve for different values of λ.

presence of a porous layer, the critical Reynolds number for the two controlled cases $\lambda = 10$ and $\lambda = 20$ are increased compared to the one of the uncontrolled case (solid case with $d = 1$). So effectively the purpose is achieved: thanks to the porous coating we have delayed the bifurcation and so the flow is stabilized. However, if it is true that on the one hand the occurrence of the bifurcation is delayed, on the other hand, we see that the trend of the curves is not monotonous. It means that if the Reynolds number is low, i.e. $Re < 50$, it is clear that for all the Reynolds in this range the porous flow is more stable with respect to the non-porous one because the growth rate of the instability is always lower ($\sigma_{porous} < \sigma_{non-porous}$). When we go beyond this range, so increasing the Reynolds number, the trend is reversed since now the growth rate of the instability is greater than the non-porous one ($\sigma_{porous} > \sigma_{non-porous}$). This behavior could be explained by two arguments : first, by increasing the Reynolds number, the non-linear effects become more important with respect to the linear ones, and secondly the term that takes into account the

porous flow (i.e. the Brinkman penalization term) is precisely a linear term. This is due to the simplicity of the Brinkman model, that model three different medium only varies the values of the dimensionless parameter λ. Finally, figure 4.28 shows the most unstable mode for the two controlled cases at $\lambda = 10$ and $\lambda = 20$. We can see clearly that the spatial distribution of the perturbation is unchanged respect with the uncontrolled case 4.18.

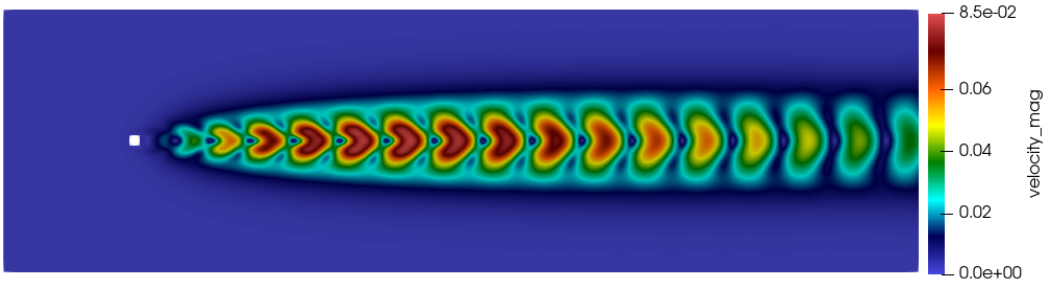

(a) Velocity magnitude $\mathbf{u}$ for the flow past a porous square cylinder for $\lambda = 10$.

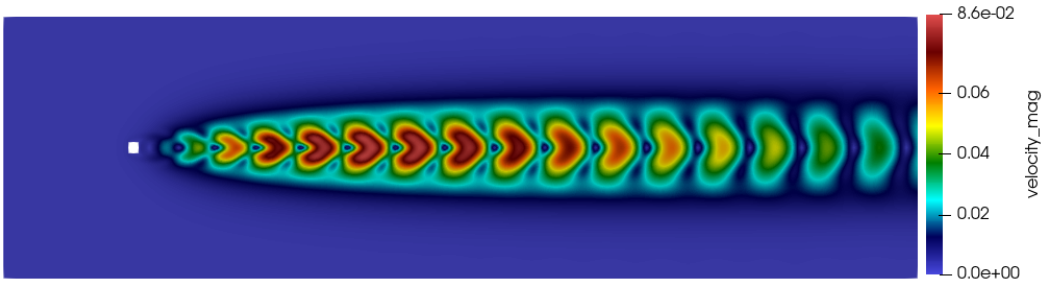

(b) Velocity magnitude $\mathbf{u}$ for the flow past a porous square cylinder for $\lambda = 20$.

Figure 4.28: Real part of the globally unstable modes associated with leading eigenvalue for the flow around a porous square cylinder at $Re = 50$.

Chapter 5

Conclusion

In this work, linear stability analysis has been performed to predict the instability of the porous flow around a square cylinder. All the simulations have been computed with the spectral element code Nek 5000. Baseflow and eigenvalues problem has been solved respectively with the selective frequency damping method and Arnoldi algorithm. To model three different media the Brinkman penalization term has been implemented in the code Nek5000. The first part has been dedicated to the stability of the non-porous flow. For the validation, the results are compared with the literature and also with internal validation, that confirms the non-linear behavior of the flow in certain configurations. Maybe one limit of this part is linked to the blockage ratio that is $\beta \simeq 4.8\%$; this value, however, doesn't alter the flow, so we don't have important blockage effects, but we could redo the study with a new β value, for example $\beta \simeq 2\%$, to reduce these effects even more. In the last part, has been performed the stability for the porous flow. For the validation, the results have been compared with the ones of the Hysop library, a validated code which also uses the Brinkman approach to perform flow control using porous media.. For all the flow configuration studied, the critical Reynolds number is inferred from the neutral curve that shows the variation of the growth rate against the Reynolds number. In, particular for the porous flow with $\lambda = 10$ and $\lambda = 20$ we have found a critical Reynolds number $Re_{\lambda=10} \simeq 46$ and $Re_{\lambda=20} \simeq 45$ that are higher than critical value of the non-porous flow. This proves that adding a porous zone around the obstacle stabilizes the flow and delays the bifurcation. The most unstable mode is unchanged respects to the non-porous flow.
This work should be a starting point to discover, for example how the position and the thickness of the porous coatings on the surface affect the flow behavior. Another interesting study, with the same spirit of this work, could be to see what happens at the second bifurcation of the flow (three-dimensional transition flow regime) when we add the porous zone on the square cylinder. In this configuration, the solid obstacle could be also a cube or a sphere.

Bibliography

[1] Nek5000 documentation. https://nek5000.mcs.anl.gov/files/2015/09/NEK_doc.pdf.

[2] P. Angot, C.-H. Bruneau, and P. Fabrie. A penalization method to take into account obstacles in incompressible viscous flows. *Numer. Math.*, 81:497–520.

[3] A. C. Antoulas. *Approximation of Large-Scale Dynamical Systems*. Society for Industrial and Applied Mathematics (SIAM), 2005.

[4] A.Sohankar, C.Norberg, and L.Davidson. Low-reynolds-number flow around a square cylinder at incidence: study of blockage, onset of vortex shedding and outlet boundary condition. *Int. J. Numer. Meth. Fluids*, 26:39–56, 1998.

[5] C.-H. Bruneau and I. Mortazavi. Passive control of the flow around a square cylinder using porous media. *Int. J. Numer. Meth. Fluids*, 46:415–433, 2004.

[6] C.-H. Bruneau and I. Mortazavi. Numerical modelling and passive flow control using porous media. *Comput. Fluids*, 37:488–498, 2008.

[7] M. O. Deville, P. F. Fischer, and E. H. Mund. *High-Order Methods for Incompressible Fluid Flow*. Cambridge University Press, 2009.

[8] P. Fischer, J. Kruse, J. Mullen, H. Tufo, J. Lottes, C. Verma, and S. Kerkemeier. website open source cfd solver nek5000. https://nek5000.mcs.anl.gov/, 2008.

[9] C. Geuzaine and J.-F. Remacle. Gmsh: a three-dimensional finite element mesh generator with built-in pre- and post-processing facilities. *International Journal for Numerical Methods in Engineering*, 79:1309–1331, 2009.

[10] H. Jiang and L. Cheng. Hydrodynamic characteristics of flow past a square cylinder at moderate reynolds numbers. *Physics of Fluids*, 30, 2018.

[11] B. E. Jordi, C. J. Cotter, and S. J. Sherwin. Encapsulated formulation of the selective frequency damping method. *Physics of fluids*, 26, 2004.

[12] K. M. Kelkar and S. V. Patankar. Numerical prediction of vortex shedding behind a square cylinder. *International Journal for Numerical Methods in Fluids*, 14:327–341, 1992.

[13] J. C. Loiseau. *Dynamics and global stability analysis of three-dimensional flows*. Phd thesis, ENSAM, Paris, 2014.

[14] P. S. Marcus and L. S. Tuckerman. Simulation of flow between concentric rotating spheres. part 2. transitions. *J. Fluid Mech.*, 185:31–65, 1987.

[15] C. Mimeau. *Conception et mise en oeuvre de méthodes vortex hybrides-frontières immergées pour des milieux solides-fluides-poreux. Application au contrôle passif d'écoulements.* Phd thesis, Université de Grenoble, 2015.

[16] C. Mimeau, G.-H. Cottet, and I. Mortazavi. Passive flow control around a semi-circular cylinder using porous coatings. *International Journal of Flow Control, Multi-Science*, 6:43–50, 2014.

[17] C. Mimeau, G.-H. Cottet, and I. Mortazavi. Passive control of the flow around a hemisphere using porous media. *European Journal of Mechanics - B/Fluids, Elsevier*, 65:213–226, 2017.

[18] A. T. Patera. A spectral element method for fluid dynamics: Laminar flow in a channel expansion. *Journal of Computational Physics*, 54:468–488, 1984.

[19] A. Roshko. *On the development of turbulent wakes from vortex streets.* National Advisory Committee for Aeronautics Report 1191, 1954.

[20] M. Toloui, A. Abraham, and J. Hong. Experimental investigation of turbulent flow over surfaces of rigid and flexible roughness. *Exp. Therm Fluid Sci.*, 101:263–275, 2019.

[21] H. Vu, J. Ahn, and J. Hwang. Numerical investigation of flow around circular cylinder with splitter plate. *KSCE J. Civ. Eng.*, 20:2559–2568, 2016.

[22] B. Zhou, X. Wang, W. Guo, W. Gho, and S. Tan. Control of flow past a dimpled circular cylinder. *Exp. Therm Fluid Sci.*, 69:19–26, 2015.

[23] E. Åkervik, L. Brandt, D. S. Henningson, J. Hœpffner, O. Marxen, and P. Schlatter. Steady solutions of the navier-stokes equations by selective frequency damping. *Physics of fluids*, 18, 2006.